J. Fluid Mech. (1996), *vol.* 329, *pp.* 275–307

Moderate and steep Faraday waves: instabilities, modulation and temporal asymmetries

By LEI JIANG[1], CHAO-LUNG TING[2]†,
MARC PERLIN[2] AND WILLIAM W. SCHULTZ[1]

[1]Department of Mechanical Engineering and Applied Mechanics, University of Michigan,
Ann Arbor, MI 48109, USA

[2]Department of Naval Architecture and Marine Engineering, University of Michigan, Ann Arbor,
MI 48109, USA

(Received 17 May 1996 and in revised form 26 July 1996)

Mild to steep standing waves of the fundamental mode are generated in a narrow rectangular cylinder undergoing vertical oscillation with forcing frequencies of 3.15 Hz to 3.34 Hz. A precise, non-intrusive optical wave profile measurement system is used along with a wave probe to accurately quantify the spatial and temporal surface elevations. These standing waves are also simulated by a two-dimensional spectral Cauchy integral code. Experiments show that contact-line effects increase the viscous natural frequency and alter the neutral stability curves. Hence, as expected, the addition of the wetting agent Photo Flo significantly changes the stability curve and the hysteresis in the response diagram. Experimentally, we find strong modulations in the wave amplitude for some forcing frequencies higher than 3.30 Hz. Reducing contact-line effects by Photo-Flo addition suppresses these modulations. Perturbation analysis predicts that some of this modulation is caused by noise in the forcing signal through 'sideband resonance', i.e. the introduction of small sideband forcing can generate large modulations of the Faraday waves. The analysis is verified by our numerical simulations and physical experiments. Finally, we observe experimentally a new form of steep standing wave with a large symmetric double-peaked crest, while simulation of the same forcing condition results in a sharper crest than seen previously. Both standing wave forms appear at a finite wave steepness far smaller than the maximum steepness for the classical standing wave and a surface tension far smaller than that for a Wilton ripple. In both physical and numerical experiments, a stronger second harmonic (in time) and temporal asymmetry in the wave forms suggest a 1:2 resonance due to a non-conventional quartet interaction. Increasing wave steepness leads to a new form of breaking standing waves in physical experiments.

1. Introduction

Standing waves can be created by reflection from coastlines, by interaction of ship-generated and ambient waves, by waves generated along the edge of a mescoscale current system, etc. Our motivation for investigating standing waves is to better interpret remotely sensed ocean surfaces, for example, those obtained by SAR (Synthetic Aperture Radar). SAR, based on the backscattering of microwaves by surface

---

† Present address: Department of Naval Architecture and Ocean Engineering, National Taiwan University, Taipei, Taiwan.

features, is sensitive to surface curvature and periodicity of the sea surface. It is generally acknowledged that standing waves can have sharper curvature than their progressive wave counterparts. Therefore, standing waves, especially capillary–gravity standing waves with length scales on the order of the Bragg wavelength, have a strong influence on both the SAR return and its interpretation.

A Faraday wave is a standing surface wave generated in a vertically oscillating container through subharmonic resonance (Benjamin & Ursell 1954). Here, we study low-mode Faraday resonance and its wave forms, especially for steep standing waves. In the Faraday experiment, spatial periodicity is better ensured by the fixed endwalls where forcing required to overcome dissipation is supplied by vertical oscillation rather than the endwall motion of Taylor (1953). Therefore the simulations and experiments on wave form are less influenced by the wave-generation mechanism. For example, Fultz (1962) compared experiments using Taylor's apparatus with analytical solutions by Tadjbakhsh & Keller (1960) and found excessive higher harmonics in the wave forms. Our experience has shown that Faraday waves provide a 'cleaner' setting for the experimental study of standing waves.

To accurately determine the wave form, especially at the crest, we excite the tank at a frequency that gives an entire wavelength within the tank. Then all our experiments are symmetric about the tank centre and a crest forms at the centreline away from the sidewall boundary layers. We shall call this the 'fundamental' mode even though the half-wavelength (slosh) mode has fewer zero-crossings. Here we emphasize three important issues that appear to be neglected in previous studies. First, the contact line not only increases effective damping, as revealed by previous studies, but also increases the natural frequency. This effect changes the neutral-stability curve and introduces hysteresis in the amplitude–frequency diagram. Second, large wave modulations observed in the experiments are explained by the influence of contact line and sideband noise in the forcing signal. Finally, different wave forms with flat or dimpled crests appear in the spatially and temporally periodic standing waves for larger forcing amplitude, accompanied by the more obvious breaking of time-reversal symmetry. These wave forms obtained by our high-resolution imaging system differ from our numerical simulations, but both experiments and simulations demonstrate strong temporal asymmetry and higher-order internal resonance.

We first review the literature on standing waves in general in §2.1. The Faraday wave and contact-line effects in particular are discussed in §2.2. The linear theory of Faraday waves is briefly described in §3.1 for later comparison. A fully nonlinear numerical method is described in §3.2, and an asymptotic analysis of the 'sideband resonance' is described in §3.3. The experimental set-up and techniques are presented in §4. In §5 and §6, the physical experiments are compared with numerical simulations and asymptotic analysis for moderate and steep waves, respectively. Preliminary experiments on breaking standing waves are shown in §7.

2. Literature review

2.1. *Standing waves*

A fifth-order standing wave solution was obtained by Penney & Price (1952) using a double Fourier series in space and time. According to their conjecture, the limiting standing wave has a wave steepness $H\lambda^{-1} = 0.218$, and a crest angle of 90°, where H is the peak-to-peak wave height and λ is the wavelength. Taylor (1953) conducted standing-wave experiments in a channel bounded at each end by a hinged-flap wavemaker. The experimental results appeared to confirm the profile and the conjectured limiting crest angle. Taylor observed that waves steeper than those of the theoretical predictions became three-dimensional and eventually broke. Schwartz & Whitney (1981) developed higher-order expansions for gravity standing waves to obtain a maximum wave steepness of $H\lambda^{-1} = 0.197$, and suggested an extrapolated maximum value of $H\lambda^{-1} = 0.208$.

A numerical investigation by Schultz & Vanden-Broeck (1990) indicated that surface tension had to be included to obtain waves as steep as those experimentally obtained by Taylor (1953). These waves had a crest sharper than 90° or had a bulbous protuberance. Penney & Price's weakly nonlinear analysis neglected surface tension and thus fortuitously predicted the maximum wave height when the expansion was extrapolated beyond the limit of its validity. For gravity standing waves, the wave period was found to be a non-monotonic function of amplitude, suggesting instability of standing waves of extreme steepness. A recent numerical study by Mercer & Roberts (1992, 1994) revealed superharmonic instability around extreme wave steepness $H\lambda^{-1} = 0.1964$. This instability corresponds to the divergence in the expansion of Schwartz & Whitney (1981) beyond the unextrapolated maximum wave steepness.

A uniqueness condition employed by Schwartz & Whitney (1981) precluded the possible resonance between the fundamental wave and higher harmonics. (For gravity waves on deep water, a series of harmonics corresponds to $1, 2, 3...$ in frequency and $1, 4, 9...$ in wavenumber.) This condition was first emphasized by Tadjbakhsh & Keller (1960) in their third-order standing wave solutions. Amick & Toland (1987) further emphasized that all symmetry conditions must be satisfied to avoid resonance in the Schwartz–Whitney solution. The symmetry conditions in space and time are

$$\eta(x,t) = \eta(-x,t) = \eta(x,-t) = \eta(-x,-t); \quad \phi(x,t) = \phi(-x,t) = -\phi(x,-t) = -\phi(-x,-t)$$

where a crest occurs at $x = 0$, $t = 0$. Previous analytical and numerical investigations have sought only temporally symmetric waves. Dissipation breaks the temporal symmetry condition, especially for steep and breaking waves. Our experiments indicate that harmonic resonances occur for steep waves, further increasing asymmetry.

A modified Zakharov equation was used by Bryant & Stiassnie (1994) in their study of multiple solutions of standing waves. The weakly nonlinear interactions between the fundamental harmonic and the resonating harmonics were considered, thus giving a family of new standing wave solutions. In particular, the second harmonic can be significant in their results, similar to our observation. However, no conditions were presented regarding the physical existence of a certain solution branch.

2.2. *Faraday waves and contact-line effects*

A review of Faraday waves was given by Miles & Henderson (1990). Of particular interest here are the single-mode Faraday wave experiments in a small circular cylinder by Henderson & Miles (1990, referred to as H&M hereafter), verifying the predictions of Miles (1984). Their experiments in a small rectangular tank did not agree as well. H&M attribute the discrepancy between the theoretical and experimental damping rates to contact-line dissipation, damping in corners (for rectangular tanks), straining of the surface film, and possible turbulent boundary layers.

For Faraday resonance, weakly nonlinear models can be derived from the averaged Lagrangian approach proposed by Miles (1976, 1984) or from direct multiple-scale analysis (Gu & Sethna 1987). Recent studies extend these models to include third-order viscous damping (Milner 1991), third-order forcing (Miles 1993) and fifth-order frequency detuning effects (Decent & Craik 1995). These improved models describe the selection of patterns in a large system with many wavelengths (Miles 1994) and include hysteresis effect (Craik & Armitage 1995).

The amplitude equation for a single-mode Faraday wave is exploited in §3.3 for periodic forcing with sideband noise to partially explain the modulation realized experimentally. Similar forcing modulation was studied by Hart (1991) for baroclinic instabilities, Ahlers, Hohenberg & Lucke (1985) for thermal convection, and Chen & Wei (1994) for bifurcation of solitary waves in shallow water. Such dynamical systems often exhibit a complicated frequency response, as demonstrated in our experiments.

The significant damping effect of contact-line hysteresis has been shown by Miles (1967) and earlier experimental studies. A composite boundary condition on the wall was proposed by Hocking (1987) and later improved by Miles (1990) to represent the damping effect at the contact line. The complex local motion near an oscillating plate at high Reynolds number was shown experimentally by Ting & Perlin (1995). However, an accurate prediction of hysteresis effects is still lacking. Contact-line hysteresis can also change the natural frequency, although this has not been explicitly discussed in the literature. The effect of a fixed contact line on the frequency of 'free' surface waves in a channel was studied first by Benjamin & Scott (1979). The eigenfrequency of the fundamental mode is significantly larger than that of a linear wave without contact-line constraint. Brimful experiments in Henderson & Miles (1994) exhibited increased viscous natural frequencies in small cylinders. Here we use the theory of Benjamin & Scott (1979) to qualitatively explain the frequency increase in our experiments with strong contact-line influence.

3. Theory and numerical formulations of standing waves

We restrict our study to two-dimensional standing gravity–capillary waves. Cartesian coordinates are attached to the wave tank with x in the longitudinal direction and the positive y-direction vertically upward from the undisturbed free surface. The free surface is represented by $y = \eta(x,t)$ and the surface tension is σ. The assumed inviscid, incompressible fluid is confined by a bottom surface at $y = -h$, and sidewalls. Subsequently, we use $k^{-1} = \lambda(2\pi)^{-1}$ as the length scale and $(gk)^{-1/2}$ as the time scale, where λ is the characteristic wavelength (the long dimension of the rectangular container) and g is the gravitational acceleration. As the fluid motion is irrotational, a velocity potential $\phi(x,t)$ satisfies

$$\nabla^2\phi = 0, \qquad -h \leqslant y \leqslant \eta, \tag{3.1}$$

$$\frac{\partial\eta}{\partial t} + \frac{\partial\eta}{\partial x}\frac{\partial\phi}{\partial x} = \frac{\partial\phi}{\partial y} \qquad \text{on } y = \eta, \tag{3.2}$$

$$\frac{\partial\phi}{\partial t} + (1 - \omega_f^2 f \cos\omega_f t)\eta + \tfrac{1}{2}(\nabla\phi)^2 = \kappa\frac{\partial^2\eta}{\partial x^2}(1+\eta_x^2)^{-3/2} - 2\gamma\phi \qquad \text{on } y = \eta, \tag{3.3}$$

$$\frac{\partial\phi}{\partial x}(x=-\pi) = \frac{\partial\phi}{\partial x}(x=\pi) = \frac{\partial\phi}{\partial y}(y=-h) = 0. \tag{3.4a,b,c}$$

Hence, the container is oscillated vertically with dimensionless displacement $f\cos\omega_f t$. The dimensionless group $\kappa = \sigma k^2(\rho g)^{-1}$ is an inverse Bond number (ratio of surface tension to gravitational forces). To obtain a steady wave amplitude independent of initial conditions and to model the experiments, dissipation using a Rayleigh-damping coefficient γ is added to the dynamic free-surface condition (3.3). If we set $f = \gamma = 0$ and impose temporal periodicity, the above formulation also applies to free standing waves as studied by Penney & Price (1952).

3.1. *Faraday waves: linear stability analysis*

Following Benjamin & Ursell (1954), the surface elevation and velocity potential are expressed as

$$\eta = \sum_{i=0}^{\infty} A_i(t) \cos k_i x, \tag{3.5}$$

$$\phi = \sum_{i=0}^{\infty} \frac{\mathrm{d}A_i}{\mathrm{d}t} \frac{\cosh k_i(h+y)}{k_i \sinh k_i h} \cos k_i x, \tag{3.6}$$

where the non-dimensional wavenumber is given by $k_i = i/2$. The primary mode (one wavelength in the tank) represented by $i = 2$ is almost exclusively studied here. Further, the linearized free-surface condition gives the Mathieu equation for $A_i(t)$,

$$\frac{\mathrm{d}^2 A_i}{\mathrm{d}u^2} + (p - 2q\cos 2u)A_i = 0 \tag{3.7}$$

where

$$u = \tfrac{1}{2}\omega_f t, \quad \omega_i = \left[k_i(1+\kappa k_i^2)\tanh k_i h\right]^{1/2} \tag{3.8a,b}$$

and

$$p = \frac{4\omega_i^2}{\omega_f^2}, \quad q = 2fk_i \tanh k_i h. \tag{3.9a,b}$$

Then the parametric resonance of Faraday waves can be interpreted in the (p,q)-plane of the Mathieu equation. Subharmonic resonance corresponds to the neighbourhood of $p = 1$ ($\omega_f \approx 2\omega_N$), where the linear stability boundary is

$$p = 1 \pm q\,, \tag{3.10}$$

for small forcing amplitude ($q \ll 1$), and ω_N is the inviscid natural frequency, as determined from equation (3.8b). The solutions to $A_i(t)$ on the neutral stability curve are periodic with frequency $\omega_f 2^{-1}$. The unstable solutions with exponentially increasing amplitude lead to finite-amplitude waves when nonlinearity or damping is considered.

Benjamin & Ursell (1954) showed that the neutral stability prediction (3.10) agrees well with experiments when the measured natural frequency is used for ω_i in the expression for p. Although the linear theory yields the stability property for a single frequency ω_i, usually the fundamental mode, with frequency ω_N, several modes can be spawned by the periodic forcing because of the nonlinear interaction among them. Various types of internal resonances in Faraday waves are reviewed by Miles & Henderson (1990). Here, we mostly study the fundamental mode ($\omega_N = \omega_2$) and compare the p,q diagram to Benjamin & Ursell (1954) and H&M based on the inviscid natural frequency in equation (3.8b). The implication of internal resonance for the steep standing waves is discussed in §6.3.

3.2. *Cauchy integral method*

When studying unsteady and steep inviscid waves, the most efficient schemes are of boundary integral type. Based on the Cauchy integral theorem for complex potentials, the Cauchy integral method is particularly effective in solving two-dimensional problems (Vinje & Brevig 1981). Convergence and efficiency of the spectral implementation are discussed in Schultz, Huh & Griffin (1994) and are not repeated here. The rudiments of the method are described in the following paragraph.

The tank walls are replaced by a horizontal periodicity condition and the semi-infinite domain of fluid is conformally mapped to an approximate unit circle for deep water waves. The periodicity condition effectively becomes a no-penetration boundary condition for the applied forcing, due to the implicit spatial symmetry in the initial conditions. The initial boundary value problem requires solutions of the complex potential $w(\xi) = \phi + \mathrm{i}\psi$ on the free surface $\xi = x + \mathrm{i}y$. The Lagrangian forms of the kinematic and dynamic conditions are applied on the free surface:

$$\frac{\mathrm{D}\xi}{\mathrm{D}t} = \frac{\mathrm{d}w^*}{\mathrm{d}\xi}, \tag{3.11}$$

$$\frac{\mathrm{D}\phi}{\mathrm{D}t} = -y[1 - \omega_f^2 f \cos(\omega_f t)] + \frac{1}{2}\left|\frac{\mathrm{d}w^*}{\mathrm{d}\xi}\right|^2 - \kappa \frac{x_s y_{ss} - x_{ss} y_s}{(x_s x_s + y_s y_s)^{3/2}} - 2\gamma\phi. \tag{3.12}$$

Here, $\mathrm{D}/\mathrm{D}t$ represents the material derivative and * denotes the complex conjugate. In the expression for surface curvature, x_s represents the derivative of x with respect to s and s is a free-surface arclength parameter.

In the Faraday wave computation, we simulate experiments using the measured damping coefficient and observe the temporal evolution of the Faraday wave rather than seeking only the temporally periodic solution. The Cauchy integral equation

$$\oint_{\partial\Omega} \frac{w(\xi)}{\xi - \zeta_k} \mathrm{d}\xi = \mathrm{i}\alpha w(\zeta_k) \tag{3.13}$$

is discretized to solve for $w(\zeta_k)$ at the kth node. Here, α is 0 or 2π if the location of the kernel singularity, ζ_k, is outside or inside the boundary, respectively. If the singularity is on the boundary, the above equation is changed to a principle-valued integral, and α is the included angle. The singularity is removed by using a Cardinal function to represent the integrand and evaluating derivatives spectrally (Schultz *et al.* 1994). At the beginning of our simulation, Lagrangian markers z_k are distributed uniformly along the free surface. At each later time step, the algebraic equations (3.13) are solved iteratively by GMRES (Saad & Schultz 1986) for the unknown part of the complex potential $w(\zeta_k)$. Equations (3.12) and (3.11) are then applied to the Lagrangian markers with a fourth-order modified Hamming predictor-corrector method to update ϕ_k and z_k.

A typical simulation of the wave amplitude evolution is shown in figure 1(*a*). The surface wave grows from a small initial disturbance to a maximum height and eventually attains the wave form shown in figure 1(*b*) with a steady amplitude. All simulations presented use 64 nodes in the horizontal direction with an error tolerance of 10^{-10} for time marching and iterative matrix solving. For this simulation, the inviscid natural frequency is 1.614 Hz, the frequency ratio $\omega_f(2\omega_N)^{-1}$ is 1.003, and a measured damping coefficient of 0.070 s^{-1} is used. The capillary effect is included although it is not a dominant factor for $\kappa = 0.00081$ (surface tension of 72 dynes cm^{-1}).

3.3. *Sideband resonance*

We have experimentally observed persistent slowly modulated wave amplitudes for forcing frequencies slightly higher than $2\omega_N$. We presume that some of the modu-

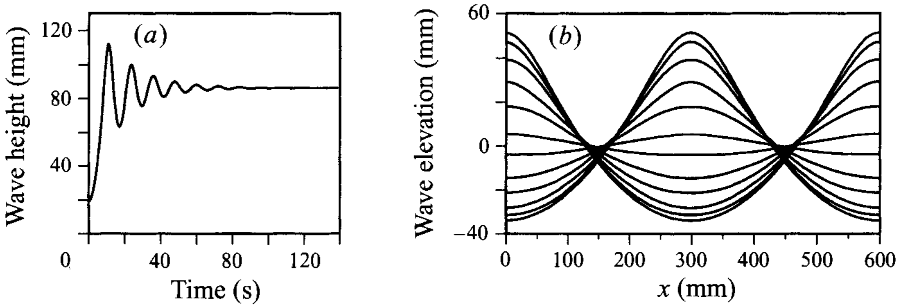

FIGURE 1. Numerical simulation of Faraday waves. (*a*) Time evolution of the wave height for a forcing frequency of 3.23 Hz and a forcing amplitude of 2.65 mm. The surface tension is 72 dyn cm^{-1}. (*b*) Wave profiles with time increment of one-eleventh of the wave period at time equal to 140 s.

lations are the result of noise in the (digital-to-analog) forcing signal and proceed to explain the modulated surface waves by perturbation analysis. We return to the discussion of sideband resonance and compare to the experiments in §5.4.

Evolution of a 2π-periodic Faraday-wave mode is described by the following amplitude equation (Miles 1984; Nagata 1989):

$$\mathrm{i}\left(\frac{\mathrm{d}}{\mathrm{d}T}+\Gamma\right)A=\Omega A+FA^{*}+G|A|^{2}A. \tag{3.14}$$

The complex amplitude $A(T)$ is assumed to be a function of the slow time scale $T=\varepsilon^{2}t$ where ε is a measure of the small surface-wave amplitude. The dimensionless parameters for frequency detuning, forcing amplitude, damping, and nonlinearity are defined respectively as

$$\Omega=\frac{\omega_f^{2}-4}{8\varepsilon^{2}},\quad F=\frac{-\omega_f^{2}f}{4\varepsilon^{2}},\quad \Gamma=\frac{\gamma}{\varepsilon^{2}},\quad G=\frac{2\tau^{4}+3\tau^{2}+12-9\tau^{-2}}{16}, \qquad (3.15a,b,c,d)$$

where

$$\tau=\tanh h. \qquad (3.15e)$$

Again, the wavenumber k and gravitational acceleration g are scaled to unity. Here, we examine deep water waves ($G>0$) and $\Omega>0$ where amplitude modulation is observed. A steady solution, $A(T)=a_0\exp(\mathrm{i}\theta)$, $0\leqslant\theta\leqslant 2\pi$, of (3.14) is

$$a_0=\left(\frac{-\Omega\pm(F^{2}-\Gamma^{2})^{1/2}}{G}\right)^{1/2}\quad\text{and}\quad \sin 2\theta=-\frac{\Gamma}{F}\geqslant 0. \qquad (3.16a,b)$$

(In Nagata 1989, $\sin 2\theta\leqslant 0$.) The dimensionless wave amplitude is described by

$$\eta_{max}=(\omega_f a_0)\varepsilon+O(\varepsilon^{2}). \tag{3.17}$$

These predictions agree with H&M and the present numerical simulation when the capillary effect is used only to modify the natural frequency.

To explain the modulations observed in experiments (e.g. see §5.4), we assume the existence of sideband noise in the forcing, i.e. the forcing amplitude is a slowly-varying function,

$$F=F_0\left[1+\beta\left(\mathrm{e}^{-\mathrm{i}t\delta}+\mathrm{e}^{\mathrm{i}t\delta}\right)\right]=F_0\left[1+\beta\left(\mathrm{e}^{-\mathrm{i}T\Delta}+\mathrm{e}^{\mathrm{i}T\Delta}\right)\right]. \tag{3.18}$$

Hence the sideband noise has relative amplitude 2β and slow frequency $\delta=\varepsilon^{2}\Delta$, with $T=\varepsilon^{2}t$. By adding modulation to the forcing signal, the amplitude equation

(3.14) becomes non-autonomous. To determine the amplification of the system by the forcing modulation, we assume a straightforward expansion for $A(T)$ as

$$A(T) = \sum_{n=0}^{\infty} \beta^n A_n(T), \tag{3.19}$$

where A_0 is the steady solution (3.16). At $O(\beta)$, equation (3.14) reduces to

$$\mathrm{i}\left(\frac{\mathrm{d}}{\mathrm{d}T} + \Gamma\right) A_1 = \Omega A_1 + F_0 A_1^* + 2G|A_0|^2 A_1 + G A_0^2 A_1^* + F_0 A_0^* \left(\mathrm{e}^{-\mathrm{i}T\Delta} + \mathrm{e}^{\mathrm{i}T\Delta}\right). \tag{3.20}$$

Since (3.20) is linear with forcing $\left(\mathrm{e}^{-\mathrm{i}T\Delta} + \mathrm{e}^{\mathrm{i}T\Delta}\right)$, $A_1(T)$ takes the following form:

$$A_1 = b_1 \mathrm{e}^{\mathrm{i}T\Delta} + b_2 \mathrm{e}^{-\mathrm{i}T\Delta}. \tag{3.21}$$

Two algebraic equations are solved in the Appendix to determine b_1 and b_2. We limit our analysis to $O(\beta)$, but the second-order correction, $A_2(T)$, can be solved in a similar way, with terms proportional to $\mathrm{e}^{2\mathrm{i}T\Delta}$.

We define the modulation amplitude of the Faraday wave as $H_{max} - H_{min}$, where H_{max} and H_{min} are the maximum and the minimum wave height (see figure 11*b*). The sideband noise amplitude is specified by the difference between the maximum and the minimum peak-to-peak tank displacement: $f_{max} - f_{min}$. The amplification factor is then expressed as

$$\frac{H_{max} - H_{min}}{f_{max} - f_{min}} = \frac{\varepsilon\,\omega_f}{2f}\left[\left(\mathrm{Re}\{b_1 + b_2\}\right)^2 + \left(\mathrm{Im}\{b_1 - b_2\}\right)^2\right]^{1/2} + O(\varepsilon^2). \tag{3.22}$$

This ratio is independent of the noise level β to this order. From equation (3.22), we define δ_{max} as the *resonant modulation frequency* corresponding to the maximum amplification. For example, if damping is neglected, the expressions for b_1, b_2 are

$$b_{1,2} = \frac{(\pm\Delta + 2F_0)F_0 a_0}{4F_0(F_0 + \Omega) - \Delta^2}. \tag{3.23}$$

The denominator goes to zero when $\delta \rightarrow \delta_{max}$ and the undamped $A(T)$ goes to infinity. For weakly damped Faraday waves, δ_{max} is relatively insensitive to the damping ratio Γ. Thus equation (3.23) gives the approximate resonant modulation frequency

$$\delta_{max} = \tfrac{1}{4}\omega_f\left\{2f\left[4 - (1 - 2f)\omega_f^2\right]\right\}^{1/2}. \tag{3.24}$$

The above estimate, limited by its lowest-order truncation and the time scale of modulation, nevertheless shows that amplified sideband noise leads to the modulation of Faraday waves. Comparison with experiments is given in §5.4. More complex phenomena like periodic doubling and chaotic motions are observed with the presence of sideband noise. We will discuss these issues in a later study.

4. Experimental apparatus and data acquisition

The dimensions of the narrow, rectangular glass tank are 600 × 60 × 483 mm (length × width × height) with an operational water depth of approximately 300 mm. This tank is constructed by adding a glass sidewall in the longitudinal direction in a wider tank 600 × 230 × 483 mm, joined at the corner by silicone. The wider tank without the added sidewall is only occasionally used to study the aspect-ratio effect on neutral stability. To help avoid contamination of the surface, the tank is scrubbed carefully before and after each use with ethyl alcohol. The rectangular tank is fixed to a platform attached to a programmable shaker with feedback control. The shaker is controlled by a Macintosh Quadra 950 computer enhanced with National Instruments' LabVIEW software and data acquisition boards. The drive motor is a brushless servo motor with a low-mass, high-performance magnequench armature. The shaker is best suited to operate in the frequency range of 0.5 Hz to 5.0 Hz. A displacement transducer and a displacement indicator monitor the vertical and lateral displacements of the tank. Throughout our experiments, the lateral displacement is always less than 3% of the vertical displacement. The excited wave field remains two-dimensional and symmetric about the centreline except when breaking occurs, in part because of the 10:1 (length to width) aspect ratio.

The spatial and temporal surface elevation data are obtained by a non-intrusive measurement technique. Figure 2 shows the high-speed-imaging system, including a 5 W Argon-Ion laser; attendant optics (a spherical lens, a cylindrical lens, and three dielectric mirrors) and a high-speed, 8-bit video system with intensified imager. As described in Perlin, Lin & Ting (1993), a laser sheet parallel to the glass front wall illuminates the central plane of the tank. Fluorescent dye (fluorescein) added to the water absorbs the chosen 488.0 nm wavelength (blue line) light and remits 550 nm (green line) light. The power output of the laser at this wavelength is approximately 0.6 W. Under the illumination of the laser sheet, no disturbance is caused by local heating as observed using surface dye motion. The optical axis of the intensified imager is oriented perpendicular to the wave direction and at about a 17° angle with respect to the mean water surface (to remove any obstructing influence from the meniscus on the front glass wall).

A Kodak Ektapro CID (charge-injection device) intensified imager and controller is coupled to an Ektapro EM 1012 processor (i.e. a controller and recorder). The image is composed of 239 horizontal pixels by 192 vertical pixels, undistorted in the two imaging dimensions. A camera lens with a focal length of 50 mm is used for the measurements. These yield an average image resolution of about 2.6 mm/pixel, determined by a precise resolution target. The estimated measurement error is about one pixel in each direction, as discussed in Perlin *et al.* (1993).

The images are taken at 250 Hz and down-loaded to the Quadra 950 via a standard GPIB interface. The smoothed wave profiles are determined by an edge-detection program with a running-average technique (Ting & Perlin 1995). The repeatability of the profile measurements is very good, as demonstrated in figure 3 for an oscillation frequency of 3.23 Hz with a stroke amplitude of 2.65 mm and a water depth of 300 mm (ω_N = 1.611 Hz). Five phases are presented in this figure; each includes three different curves. The solid and the dashed curves represent the results of two consecutive periods of the same experiment. The dotted curves are from a separate experiment with the same operational conditions.

Three different test fluids are used: treated water, treated water with fluorescein dye and treated water mixed with Photo Flo 200 in the volume ratio of 100:1. Here, the water treatment systems include a 5 μm particulate pre-filter, a de-ionization tank, a carbon adsorption phase and a 0.2 μm particulate final filter. At a room temperature of 23°C, the static surface tension measured by a CSC-DuNoüy tensiometer is about 72 dynes cm^{-1} for treated water. For the water treated with Photo Flo, the surface tension drops to 38 dynes cm^{-1} immediately after the addition of Photo Flo, but decreases to a steady value of 31.6 dynes cm^{-1} in approximately 15 minutes. These measurements are consistent with surface-tension measurements of very high-quality

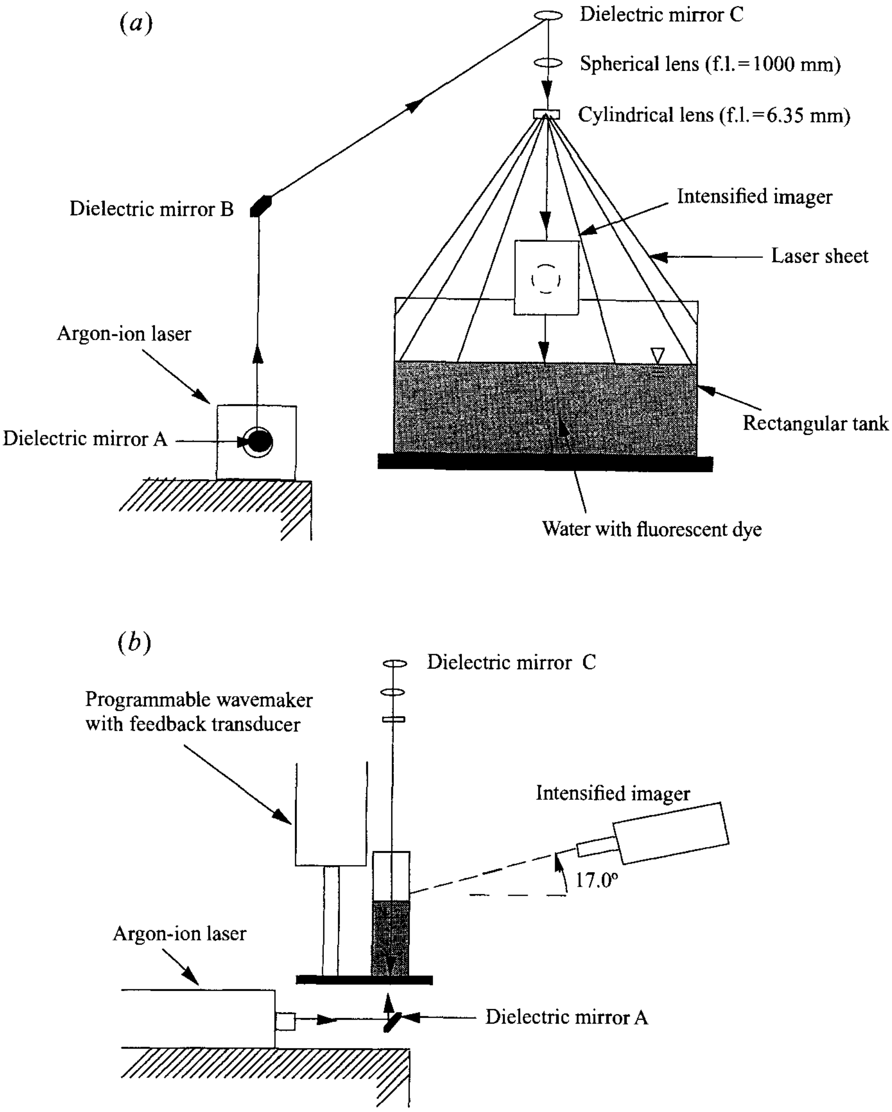

FIGURE 2. A schematic of the high-speed-imaging measurement system: (*a*) front elevation, (*b*) side elevation.

HPLC (high-pressure liquid chromatography) water and HPLC water with Photo Flo that are used as a benchmark.

Instantaneous wave elevation at a particular station can be determined from images of the profile. However, discussion of the damping rate and hysteresis is based on wave-gauge measurements. We used a capacitance-type wave probe with an outside diameter of 1.6 mm to measure the surface displacement at the horizontal centre of the tank. The measurement error is less than 1% of the wave height. Detailed discussion of the wave probe can be found in Perlin & Hammack (1991). The probe and feedback signals are filtered using two Krohn-Hite model 3342 analog filters with a cutoff frequency of 30 Hz. The filter does not affect the amplitude and phase of the spectral components in the frequency

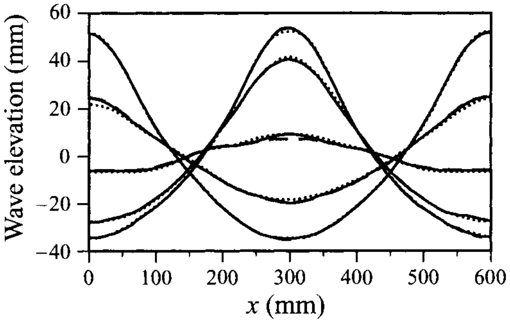

FIGURE 3. Repeatability of Faraday-wave experiments for a 3.23 Hz oscillation with a forcing amplitude of 2.65 mm: —— and — —, represent profiles from two consecutive periods of the same experiment; ······ represents the results obtained on a different day, but with the same operational conditions.

range of our interest: 0–10 Hz. These signals are digitized at 200 Hz; then, the feedback signal is subtracted from the probe signal to obtain the actual surface displacement.

The damping rate is determined as follows. The tank is oscillated at constant frequency with constant stroke amplitude. After waves attain stationary periodic motion, the shaker motion is stopped and surface displacement at the tank centre is recorded for 20 s with a sampling frequency of 50 to 100 Hz. The corresponding wave damping rate is calculated by curve fitting the measured crest-to-trough wave heights.

To determine the neutral stability curves, the tank is oscillated at a constant frequency and amplitude for a minimum of three minutes. The forcing amplitude is increased until a Faraday wave is generated. This amplitude is termed the threshold forcing amplitude, accurate to the amplitude increment: 0.05 mm. The *viscous natural frequency* ω_v is defined as half of the forcing frequency that corresponds to the minimum threshold forcing amplitude (q_{min} in dimensionless form). The p associated with q_{min} is designated p_{min}. From experimental observation, with $\omega_f < 2\omega_v$ ($p > p_{min}$), determination of the subharmonic resonance is rather straightforward as a jump from the null state to a finite wave amplitude occurs. On the other hand, with $\omega_f \geqslant 2\omega_v$ ($p \leqslant p_{min}$), the amplitude of the Faraday waves increases gradually from a low level so the more subtle change is difficult to detect. Therefore care is required to ensure that oscillations from previous testing have decayed to a quiescent level, especially for the latter case. We must allow sufficient time for the instability to develop for $\omega_f < 2\omega_v$ and carefully observe the small-amplitude subharmonic component in the wave spectrum for $\omega_f > 2\omega_v$.

To obtain the hysteresis effect in the amplitude–frequency diagram, experiments with increasing and later decreasing oscillation frequencies are conducted for each forcing amplitude. The shaker-control algorithm maintains a constant amplitude oscillation while varying frequency in small, discrete steps. Six to ten different frequencies are chosen for a 30 minute experiment; therefore, each frequency is held constant for 3 to 5 minutes. The difference between successive frequencies is in the range of 0.01 to 0.025 Hz. The resonant waves reach stationary periodic motion after about 150 s and a 5 s elevation record is recorded to determine the wave amplitude.

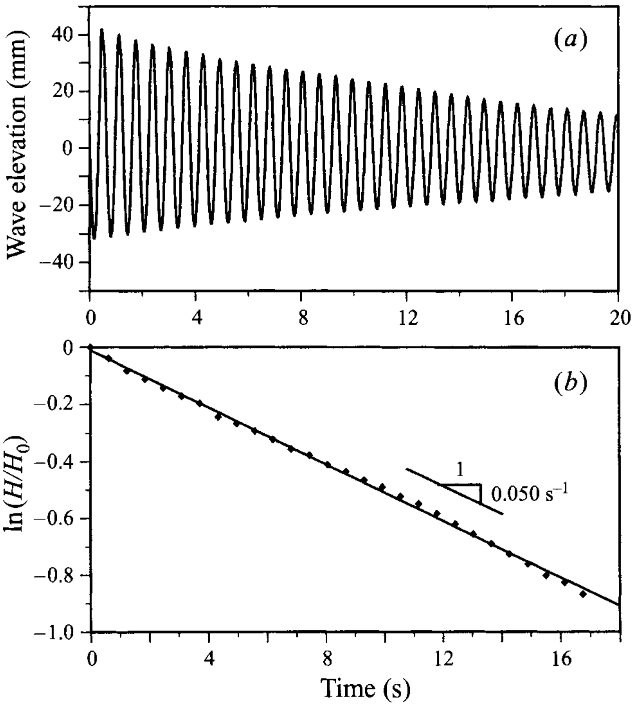

FIGURE 4. A damping–rate measurement at forcing frequency 3.23 Hz and forcing amplitude 2.65 mm with an operational water depth of 300 mm. (*a*) A time series of wave elevations at the horizontal centre of the container. (*b*) A graph of the wave-height decay where 0.050 s^{-1}, the slope of the linear curve fit, represents the damping rate. H is the measured wave height, and H_0 is the initial wave height.

5. Faraday waves: small to moderate amplitude

5.1. *Damping rate and elevation profiles*

We found the theoretical damping rate predictions of H&M to be inadequate, as did they. Therefore, measured linear damping rates are used in the weakly nonlinear theory and numerical estimates when comparing with experiments. As described in §4, a typical damping-rate measurement is presented in figure 4, with treated water, a 10:1 tank aspect ratio, a forcing frequency of 3.23 Hz, and an initial forcing amplitude of 2.65 mm. Part (*a*) is a time history of wave elevation at the horizontal centre of the container after the forcing is discontinued. Linear curve fitting (log amplitude–linear time) in figure 4(*b*) estimates a damping rate of 0.050 s^{-1}. Unless otherwise specified, this is the damping rate used in our numerical experiments. A series of damping-rate measurements with an aspect ratio of 10:1 shows that the damping rate of 0.050 s^{-1} increases to 0.058 s^{-1} when the treated water is mixed with Photo Flo (100:1), and that of water mixed with fluorescein dye is 0.070 s^{-1}. These measurements also appear to apply to the steep waves discussed in §6.

As a first comparison between numerical and physical experiments, and a (partial) validation of the numerical code, figures 1(*b*) and 3 are revisited. An oscillation frequency of 3.23 Hz with an oscillation amplitude of 2.65 mm is used in both experiments. A measured damping rate of 0.070 s^{-1} is used in the numerical simulation as the container is filled with a water–fluorescein mixture. As is seen by comparing the figures, the numerical simulation predicts the measured profiles very well.

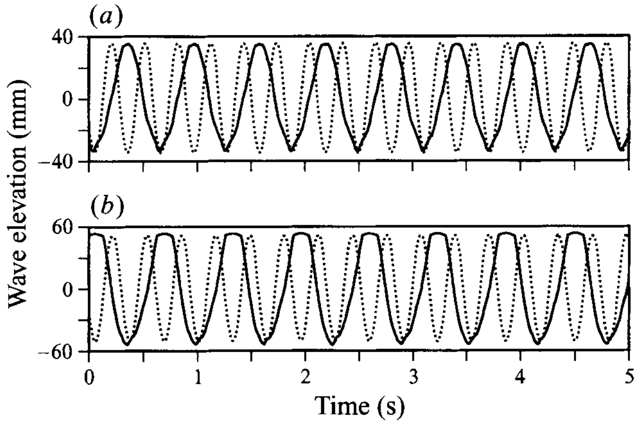

FIGURE 5. Experimental records of phase information for resonant waves and wavemaker position: ——, wave elevation signal at the tank centreline; ······, vertically exaggerated shaker position signal. The forcing frequencies of the records are 3.27 Hz (*a*) and 3.15 Hz (*b*). Graphs (*a*) and (*b*) are recorded during experiments with incrementally increasing and decreasing frequency, respectively.

5.2. *Subharmonic instability*

5.2.1. *Phase of the Faraday waves*

In subharmonic resonance, the phase between the forcing motion and the resonant waves is important. The forcing motion inputs energy to the dissipative system when the tank acceleration supplements gravity (tank acceleration opposite to gravity) and the trough-to-peak wave displacement is close to a maximum. Hence, experiments show that the trough and crest phases of the resonant waves are approximately in-phase with consecutive troughs of the forcing signal.

Two experimental records are shown in figure 5 with forcing frequencies of 3.27 Hz and 3.15 Hz, both with the same forcing amplitude of 2.65 mm. Note that the wave-probe measurement in figure 5(*b*) has a flat wave-elevation trace in time. This is simply a feature of the steep-wave form as discussed in §6. In the figure, the forcing signal is scaled so that its peak-to-peak value matches that of the wave elevation. Our experiments show that the phase of the forcing signal trough lags the wave trough by 9° to 17°, and the phase of the forcing signal trough precedes the wave crest by 0 to 6°. The phase lags are based on the wave (not the forcing) period and its relatively small magnitude is in qualitative agreement with our numerical simulation and weakly nonlinear theories, Miles (1984) for example.

5.2.2. *Neutral-stability diagram*

The threshold forcing amplitude of several forcing frequencies is measured and a stability diagram is presented in figure 6 for three slightly different fluids and two tank aspect ratios. Also shown is the Faraday wave with two wavelengths in the tank ($k_i = k_4 = 2$). This mode is generated by a higher forcing frequency ($\omega_f \approx 2\omega_4 \approx 2\sqrt{2}\omega_2$) so the resonance is still subharmonic. Figure 6(*a*) presents results from the measurements of water and mixed water with fluorescein dye and figure 6(*b*) for water mixed with Photo Flo 200, volume ratio 100:1. Dimensionless frequency p and dimensionless forcing amplitude q are evaluated using (3.9*a*, *b*) based on the inviscid natural frequency ω_N. If p and q lie within the upper and lower solid diagonal lines (unstable region), then subharmonic resonance will occur according to

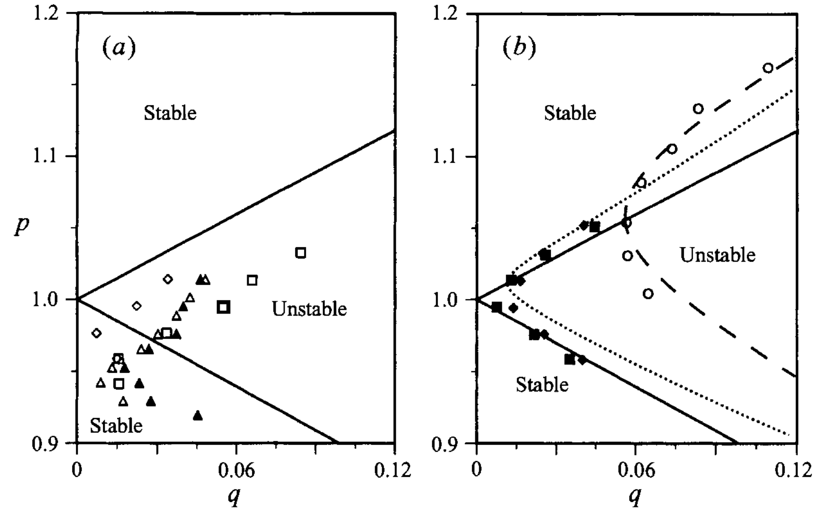

FIGURE 6. Subharmonic-instability limit data from experiments with (*a*) treated water, (*b*) treated water mixed 100:1 with Photo Flo. ▲◆, Tank aspect ratio 10:1; ▲, tank aspect ratio of 10:1 (two 30 cm wavelengths in tank); ◇■, tank aspect ratios are 2.61:1; □, treated water mixed with fluorescent dye, tank aspect ration of 10:1 ($\sigma = 71$ dyn cm^{-1}); ○ experimental data from H&M with 80:1 water–Photo Flo mixture ($\sigma = 42.3$ dyn cm^{-1}). ——, Inviscid subharmonic-instability curves; — —, instability curve from H&M to predict their experimental results; ······, instability curve from H&M for our experimental conditions.

the inviscid theory of Benjamin & Ursell (1954); otherwise, the liquid surface is not excited (stable region). The dashed curves represent predictions using the theory of H&M.

According to H&M, the viscous natural frequency ω_v, that associated with p_{min}, should be less than the inviscid natural frequency ω_N. However, our experimental results show an increase in ω_v, not a decrease. As shown in figure 6(*a*), the p_{min} associated with each set of symbols is less than 1, implying that $\omega_v(\equiv \frac{1}{2}\omega_f|_{q_{min}}) > \omega_i$. Benjamin & Scott (1979) measured waves propagating in a brimful channel and concluded that the contact-line effect increases the wave celerity (phase speed). We believe this same phenomenon is responsible for our increased ω_v with fixed wavenumber. (Note that they measured much greater increases than measured here, presumably because of the extended width of our tank and the stronger constraint of the contact line in their study.) By reducing the tank aspect ratio and by the addition of Photo Flo, thus lessening the relative effect of the contact line, we now demonstrate that this conclusion is warranted.

The aspect-ratio effect on the frequency is seen in figure 6(*a*) by comparing measurements in the wider tank (aspect ratio 2.61:1) and those in the narrow tank (aspect ratio of 10:1). Owing to a weaker contact-line effect in the wider tank, ω_v should be and is smaller, corresponding to an increase in p_{min}. Also, since the contact line and wall boundary layers contribute the most to the dissipation, the effective damping in the wider tank is less due to the smaller surface-area-to-volume ratio. Therefore q_{min} in the wider tank is smaller.

Figure 6(*b*) represent our measurements with the mixture of water and Photo Flo. Since the addition of Photo Flo reduces the contact-line effect, p_{min} and q_{min} are now more affected by viscous damping and the neutral-stability curve shifts towards H&M's prediction. H&M's theory still overpredicts q on the lower side of the neutral-stability curve and underpredicts ω_v. Their experiments (hollow symbols) agree with their theory quite well. Since they conducted experiments with a Photo-Flo mixture in a smaller container, 88.70 × 32.05 × 10 mm, viscous damping in their system has a more dominant effect so both p_{min} and q_{min} are larger. (The ratios of the total surface area to the volume are 0.40 and 1.85 for our tank and H&M's cylinder respectively.)

Miles (1967) and Milner (1991) stated that contact-line hysteresis makes an important contribution to the total damping. There is also a difference between the static contact-line damping encountered in infinitesimal waves, and the dynamic contact-line damping for finite-amplitude waves as found in the damping measurements. For treated water, the measured damping rate is $0.085\,\mathrm{s}^{-1}$ when two wavelengths are present. (In this case only we used 4.68 Hz forcing to excite two wavelengths in the tank.) For the fundamental mode, the damping rate is $0.05\,\mathrm{s}^{-1}$. The ratio (second:fundamental) of dimensionless damping rates is then 1.20 for these two modes. From figure 6(*a*), the dimensionless threshold forcing associated with two wavelengths ($q_{min} = 0.0177$) is approximately twice that for the single wave ($q_{min} = 0.0087$). As q_{min} is proportional to the dimensionless damping rate, it implies a larger damping-rate ratio than the 1.20 from the direct damping measurement. For the initiation of waves (infinitesimal waves), the contact line plays a more dominant role than it does with finite-amplitude waves. This is due to a fixed contact line for very small waves when the contact angle is within the advancing and receding contact angles ('stick' motion described in Ting & Perlin 1995), while the contact line exhibits stick-slip motion when the wave amplitudes (and hence contact angles) are large.

5.3. *Response diagram and hysteresis effects*

Weakly nonlinear predictions were validated in H&M by experiments in small cylinders. However, individual experiments were conducted using a fixed forcing frequency and amplitude with a calm-water initial state. Hysteresis (of the soft-spring type) in the limit-cycle amplitude is determined from changing the forcing frequency in steps without returning to quiescent conditions.

Figure 7(*a*) shows the Faraday wave amplitude as a function of the forcing frequency in our 10:1 aspect-ratio rectangular tank for three forcing amplitudes: 2.5 mm, 3.0 mm, and 3.5 mm. The arrows denote the response of amplitude to the direction of frequency change. Solid/hollow symbols represent the experiments with increasing/decreasing frequency, started from the upper/lower side of the unstable regions in the p, q diagram. For increasing forcing frequency, the response curves (dashed lines) exhibit abrupt changes from zero to a finite amplitude. The frequency ratio where the jump occurs is larger for smaller forcing amplitude: 1.002 for 2.5 mm, 0.992 for 3.0 mm, 0.982 for 3.5 mm forcing. The response curves, starting from the right of the unstable region, bypass the jump positions and increase until incipient breaking of the Faraday wave occurs.

The contact line causes this single-mode hysteresis by shifting the jump positions and the neutral-stability curve. In the p, q diagram, figure 7(*b*), solid/dashed lines with arrows represent excited Faraday waves with decreasing/increasing forcing frequencies, corresponding to the solid/dashed lines in figure 7(*a*). By starting the forcing frequency from the left of the backbone curve in figure 7(*a*), the experiment approaches the neutral-stability curve from above (dashed arrow in figure 7*b*). Owing to the contact-line constraint (without the lubrication of Photo Flo), the viscous natural frequency is larger and the neutral-stability curve is shifted downward in figure 7(*b*) (dashed curve). This corresponds to a rightward shift in the jump position in figure 7(*a*). When the forcing frequency approaches the jump position from the right of

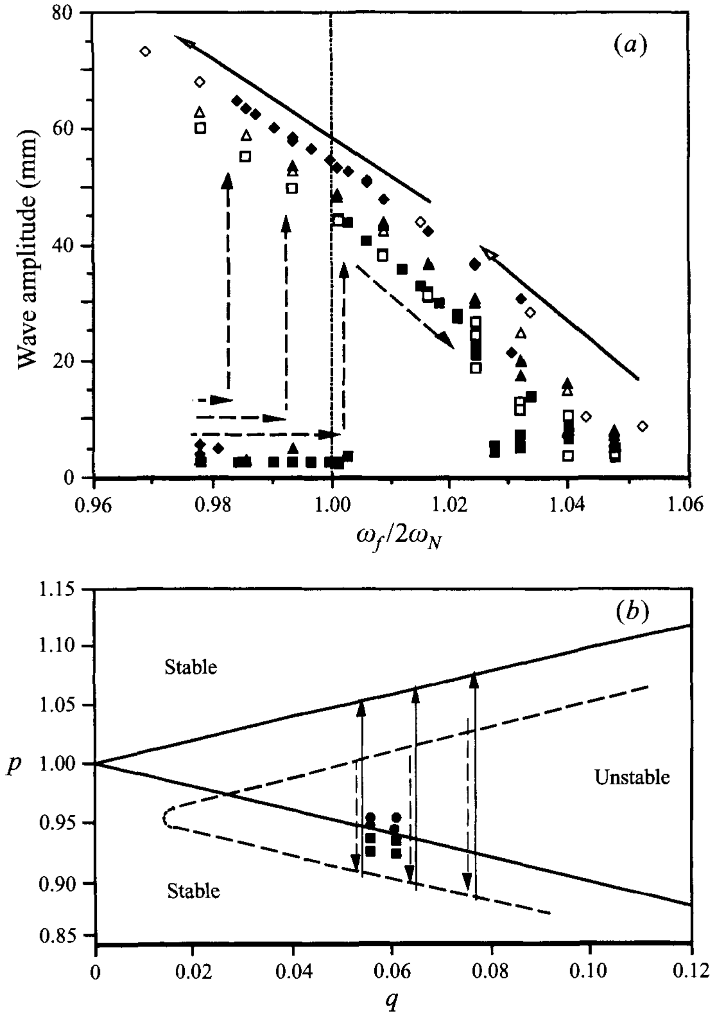

FIGURE 7. (*a*) Faraday-wave amplitudes for varying forcing frequencies. Solid symbols represent frequencies varied in small steps from low to high frequency at constant forcing amplitude. Hollow symbols represent frequency variations in the opposite direction. Three forcing amplitudes are used: 2.5 mm (■ and □), 3.0 mm (▲ and △), and 3.5 mm (◆ and ◇). (*b*) The path of the same experiments in the p, q diagram. Solid/dashed lines with arrows represent excited Faraday waves with decreasing/increasing frequency shown in (*a*). Inviscid and measured neutral–stability curves are given by —— and — —, respectively. Solid circles and squares represent the appearance of modulation as discussed in §5.4.

the backbone curve, the Faraday wave gradually grows to a finite amplitude. The static contact line that inhibited the infinitesimal or low-amplitude wave no longer affects the Faraday excitation when the forcing frequency is further reduced, passing the jump position. So rather than a return to the quiescent state, the wave amplitude keeps growing with decreasing forcing frequency until breaking occurs.

We show in figure 8 the frequency response of the limit-cycle wave amplitudes for treated water versus that for treated water with Photo Flo. In figure 8(*a*), H&M's theoretical predictions agree qualitatively with our experiments with a forcing amplitude of 2.5 mm, except for the jump position. Wave amplitudes estimated by our fully nonlinear simulations agree better with the experiments over most of the

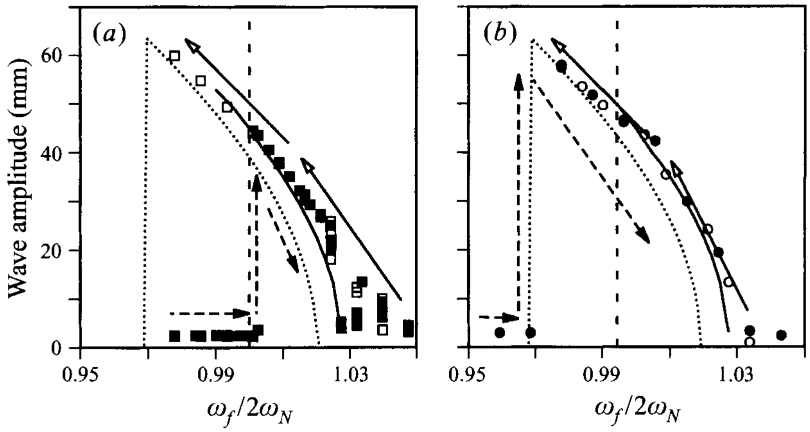

FIGURE 8. Faraday-wave amplitudes for varying forcing frequencies at a forcing amplitude of 2.5 mm: ······, H&M's theory with our measured damping rate; ——, numerical results. (*a*) Experiment conducted with treated water: ■ and □ represent the data measured with increasing and decreasing frequencies, respectively. (*b*) Experiment conducted using treated water with Photo Flo in a ratio 100:1: ● and ○ represent the data measured with increasing and decreasing frequencies, respectively.

frequency range. Figure 8(*b*) shows that the addition of Photo Flo changes the jump position significantly. With reduced contact-line effects, the resonance curve, particularly the jump position, is closer to the theoretical prediction of H&M and inviscid analysis.

Similar hysteresis was observed by Dodge, Kana & Abramson (1965), who also indicated a slight increase in the viscous natural frequency ω_v. H&M predicted different jump positions and observed no evident hysteresis, as did Virnig, Berman & Sethna (1988). Note that the hysteresis shown here is not due to the available zero- and finite-amplitude solutions for the same forcing parameter. That type of hysteresis exists outside the theoretical neutral-stablity curve (to the left of the dotted vertical lines in figure 8) as discussed in detail by Decent & Craik (1995). The present experiments do not proceed beyond the theoretical neutral-stability curve because of strong wave breaking.

5.4. *Sideband resonance*

Comparison of figures 8(*a*) and 8(*b*) shows that on the high-frequency side of the backbone, better agreement with the numerical estimates is achieved by doing experiments with the mixture of water and Photo Flo, i.e. with reduced contact-line and surface-tension effects. A similar 'tail effect' was also observed by Virnig *et al.* (1988), i.e. the wave amplitude does not decay as rapidly to zero as the theory for increasing excitation frequency. They ascribed it to the effect of capillarity and removed the tail using Photo Flo. Based on our experiments, the contact line significantly changes the natural frequency; therefore, we expect that the tail is also due to the contact-line effect, rather than a mere surface-tension effect.

In fact, our measurements show large modulations in the time series of the wave amplitude in the tail region where $1.02 < \omega_f(2\omega_N)^{-1} < 1.05$. Figure 9(*a*) shows the probe measurement with its spectrum for a forcing amplitude of 2.90 mm, a forcing frequency of 3.30 Hz. A sideband frequency of 1.60 Hz is measured so the modulation frequency is 0.05 Hz. The magnitude of the modulation is even more significant in figure 9(*b*) with a modulation frequency of 0.03 Hz. The modulations exist in both the experiments with stepped varying frequency and those starting from a quiescent state. As we estimate the amplitude by averaging the maxima of probe signal in a 5 s window, the slow modulation causes random deviations of the wave amplitude in the tail regions of figure 7(*a*) and figure 8(*a*).

No modulation is observed in our fully nonlinear numerical simulations, even with higher harmonics in the sinusoidal forcing. Hence, the effect of higher harmonics in the forcing signal (figure 9) is minimal because of their small magnitudes (less than 1–2% of the forcing amplitude). However, using the experimental forcing signal as the numerical input does cause modulation, albeit with less magnitude. Since no contact-line effect is simulated, it suggests two factors causing the modulation: contact-line effect and sideband noise in the forcing signal. There is a certain degree of uncertainty in our observation of modulation. Recent repeated experiments to reproduce figures 9 and 10 show no observable modulations for the same forcing parameters. Change in the natural background noise is likely to be the reason, perhaps due to the completion of nearby construction.

Decent & Craik (1995) proposed a different mechanism. According to them, nonlinear forcing and damping can cause hysteresis in the neutral-stability diagram and limit-cycle behaviour in the wave amplitude. However, in applying their criterion to our experiments, the modulation should mostly occur to the left of the backbone curve, with only a slight possibility of limit-cycle response on the high-frequency side. We see from the following discussion that the contact-line effect and random nature of the sideband noise are more important here than nonlinear damping.

5.4.1. *Modulation frequency*

Usually, the bandwidth of the forcing signal is narrow and its effect on wave modulation is not seen. However, from (3.24), the resonant modulation frequency δ_{max} decreases with increasing forcing frequency, eventually to within the effective bandwidth of the forcing signal. Owing to the large amplification of the forcing noise on the high-frequency side of the backbone curve, the wave modulation is then visible. Faraday-wave modulation as shown in figure 9 can be measured by its frequency and amplitude. Since the theory in §3.3 typically considers paired sidebands and the experiments have continuous sidebands, we can only compare the observed modulation frequency with the prediction of δ_{max} in (3.24).

In figure 10, four experiments with modulation frequency between 0.037 Hz and 0.05 Hz agree reasonably well with our prediction, even without the full details of the forcing noise. In six other experiments, we measured modulation frequencies between 0.02 Hz and 0.032 Hz, while the analysis predicts nearly no modulation. The discrepancy is explained again by the frequency shift due to the contact line. Figure 7(*b*) clearly indicates that the forcing parameters for these six cases (squares) are already on the stable side of the inviscid p, q boundary. However, the contact-line effect shifts the neutral-stability curve downward so that these experiments are still within the unstable region. As the experiments proceed toward the lower stability boundary, the wave amplitude becomes smaller and the contact-line effect strengthens. The present analysis does not account for contact-line effects, therefore it is unable to predict the observed modulations for the six experiments.

5.4.2. *Modulation amplitude with controlled sideband noise*

To verify the sideband-noise amplification quantitatively, we use controlled sideband noise in both experiments and numerical simulations. Without added sideband noise, the Faraday wave from physical experiments is steady with a forcing amplitude

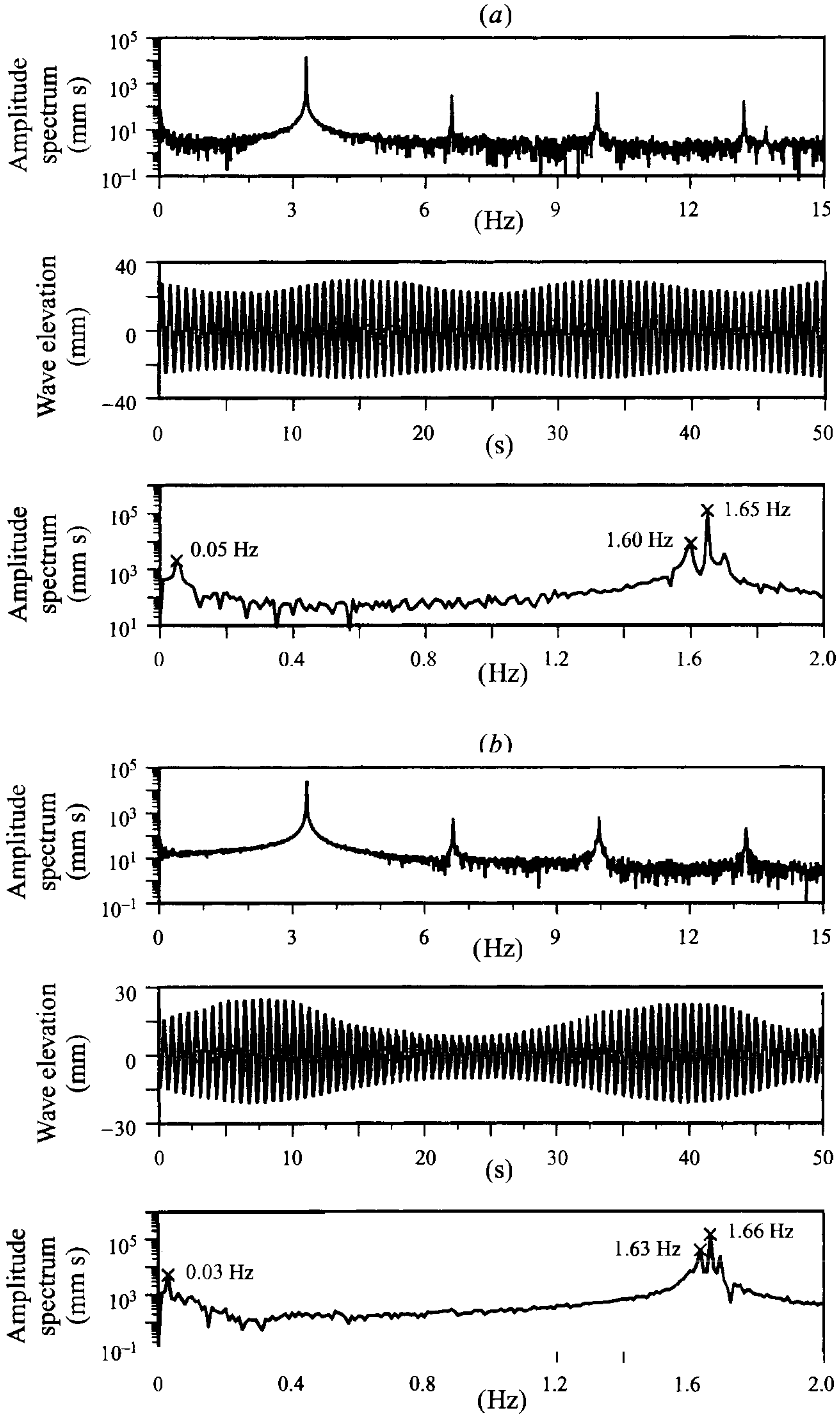

FIGURE 9. Two cases of steadily modulated Faraday waves. (*a*) A 3.30 Hz oscillation with forcing amplitude = 2.90 mm. (*b*) A 3.32 Hz oscillation with forcing amplitude = 2.65 mm. The top graph in (*a*) and (*b*) is the forcing-signal spectrum, the second graph is a time series of wave elevation at the horizontal centre of the tank, and the third graph is the amplitude spectrum of the wave-probe signal.

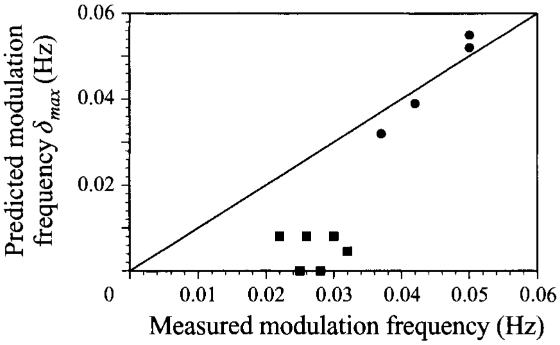

FIGURE 10. Comparison of the predicted δ_{max} with the modulation frequencies in the experiments with forcing frequency between 3.30 Hz and 3.34 Hz, forcing amplitude of 2.9 mm and 2.65 mm. Solid circles and squares are the same as those shown in figure 7(*b*).

of 2.65 mm and a forcing frequency of 3.23 Hz (figure 11*a*). After 5% double-sideband noise is added to the forcing signal, the wave elevation, figure 11(*b*), has the same modulation frequency as the sideband noise in the forcing signal, 0.09 Hz, but the modulation magnitude is increased dramatically compared to the small noise level in the forcing signal. Here, we define the controlled noise level as the ratio of each sideband-frequency amplitude to the amplitude of the primary frequency component.

The effect of the detuning frequency δ is shown for several amplitudes at each of the two sideband frequencies and two forcing frequencies 3.23 Hz and 3.27 Hz in figure 12. The prescribed noise levels are 1.0%, 2.5%, 3.75%, and 5% of the basic forcing amplitude of 2.65 mm. The detuning frequency associated with the largest modulation amplitude is independent of the sideband amplitude. The normalized modulation magnitude shown in figure 12(*b*) is also independent of the sideband amplitude, but has slight changes for the different forcing frequencies. All these observations are consistent with predictions from equation (3.22). Another interesting feature is the unbalanced sidebands in the wave spectrum as shown in figure 9(*a*, *b*) and especially figure 11(*c*). The amplitude associated with the lower frequency $(\omega_f 2^{-1} - \delta)$ is always larger than the amplitude associated with the upper frequency $(\omega_f 2^{-1} + \delta)$. The same conclusion is drawn from the solutions for $b_{1,2}$, even with zero damping rate in equation (3.23).

In figure 13, the predicted amplification factor exhibits reasonable agreement with experimental results for different sideband frequencies. Noise is amplified as much as 45 times, leading to obvious modulations in the Faraday waves. Numerical results with added sideband frequency components agree very well with the theory, except at $\delta = 0.15$ Hz in figure 13(*b*). At this frequency, we observed period doubling that is not predicted by our first-order analysis. In both (*a*) and (*b*), the asymptotic analysis agrees reasonably well with physical experiments for larger δ, but less satisfactory as $\delta \to 0$. A discrete Fourier transform (DFT) of the feedback signal shows a forcing spectrum of finite bandwidth when δ goes to zero, so the added sideband noise cannot be well represented by the asymptotic analysis with a discrete noise spectrum. Nevertheless, the predicted resonant modulation frequency δ_{max} is consistent with the maximum amplification from numerical and physical experiments.

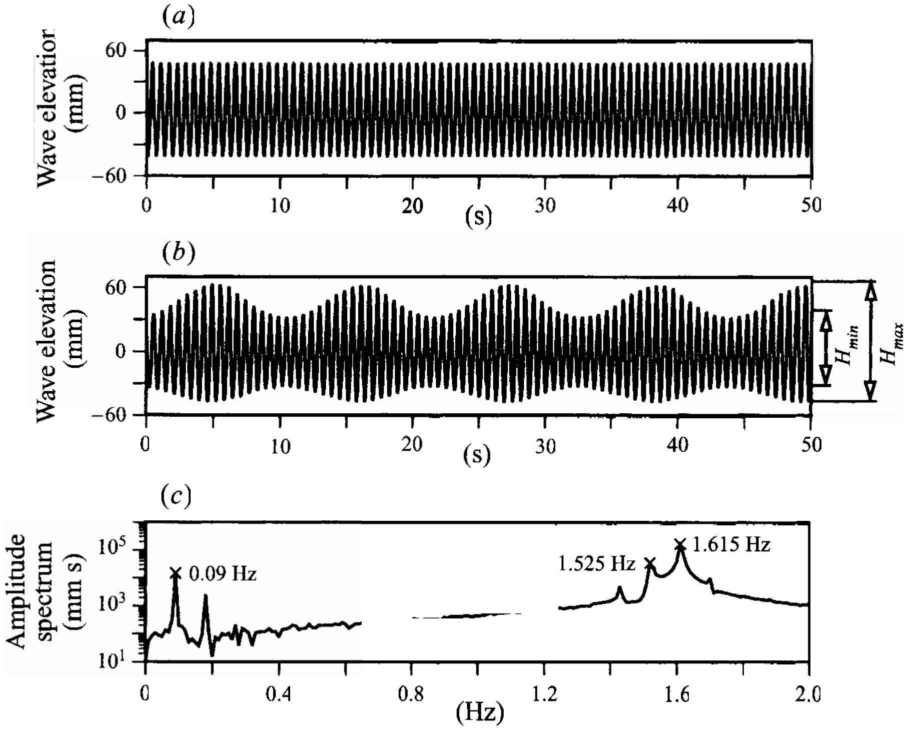

FIGURE 11. Steadily modulated Faraday waves obtained by intentionally adding sideband noise to the forcing. The oscillation frequency is 3.23 Hz, forcing amplitude is 2.65 mm. (*a*) Wave elevation without additional sideband noise. (*b*) Wave elevation with 5% sideband noise on both sides of the primary forcing frequency, detuning frequency $\delta = \pm 0.09$ Hz. (*c*) The amplitude spectrum of the wave-probe signal shown in (*b*).

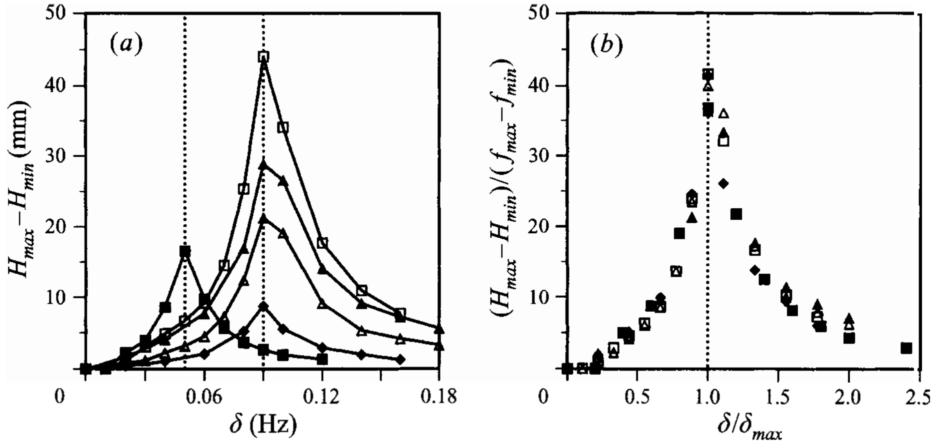

FIGURE 12. The effect of detuning frequency on the modulated wave heights with 2.65 mm forcing amplitude. (*a*) Dimensional graph: ■, 2.5% sidebands with 3.27 Hz oscillation; □, 5% sidebands with 3.23 Hz oscillation; ▲, 3.75% sidebands with 3.23 Hz oscillation; △, 2.5% sidebands with 3.23 Hz oscillation; ◆, 1% sidebands with 3.23 Hz oscillation. The vertical dashed lines correspond to the observed maximum wave modulation. (*b*) Non-dimensional graph, where $f_{max} - f_{min}$ is the peak-to-peak modulated forcing amplitude and δ_{max} is the measured detuning frequency corresponding to the maximum modulated wave height. Symbol representations are the same as in (*a*).

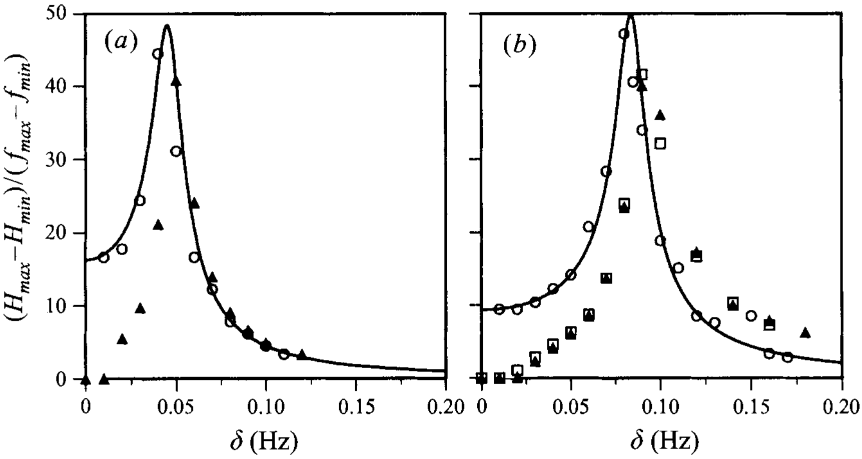

FIGURE 13. Sideband amplification with intentional sideband noise: ——, first-order analysis (3.22); ○, numerical simulation with 5% side bands; ▲, experiments with 2.5% side bands; □, experiments with 5% side bands. $H_{max} - H_{min}$ is the modulation amplitude of the Faraday wave and $f_{max} - f_{min}$ is the modulation amplitude of the forcing signal. (*a*) Forcing frequency of 3.27 Hz with forcing amplitude of 2.25 mm. (*b*) Forcing frequency of 3.23 Hz with forcing amplitude of 2.65 mm.

5.4.3. *Single-sideband controlled noise*

In the asymptotic analysis, double-sideband noise is added to the slowly modulated forcing amplitude. However, both sidebands need not be present. Experimental results in figure 14 imply that a single sideband added on the lower side of the primary frequency component causes most of the modulation, while the upper sideband noise has very little effect. As shown in the response diagram, figure 7(*a*), the Faraday wave grows when the forcing frequency decreases from the higher-frequency side of the backbone curve. Hence, the lower sideband corresponds to a stronger resonance effect and causes large modulations. By contrast, adding an upper sideband component introduces an additional higher forcing frequency that has little or no resonance effect. This observation agrees with our numerical simulations.

5.4.4. *Contact line*

We have demonstrated that even in the absence of the contact line and surface-tension effects, amplification of sideband forcing noise occurs. The addition of Photo Flo in any experiments when sideband modulation is apparent, whether by the intentional addition of small sidebands in the forcing signal or not, causes the modulation to greatly diminish. With Photo Flo present and the modulations essentially removed, the forcing signal is altered further by increasing the sideband forcing. The modulations in the Faraday waves reappear, again with large amplification. This then shows that the existence of the contact line increases the background perturbations (i.e. the noise floor) and acts as a catalyst to precipitate the large modulations. Of course, as opposed to the non-monochromatic forcing signal, the contact-line effects are due to fluid dynamics and directly cause modulation of the Faraday waves. A complete study of this phenomenon along with the effect of contamination is required to quantify the processes.

5.5. *Temporal asymmetry*

As defined in §1.2, time-reversal symmetry means that the surface elevation at $t_0 - t$ is the same as that for $t_0 + t$, where t_0 represents the instant of maximum elevation

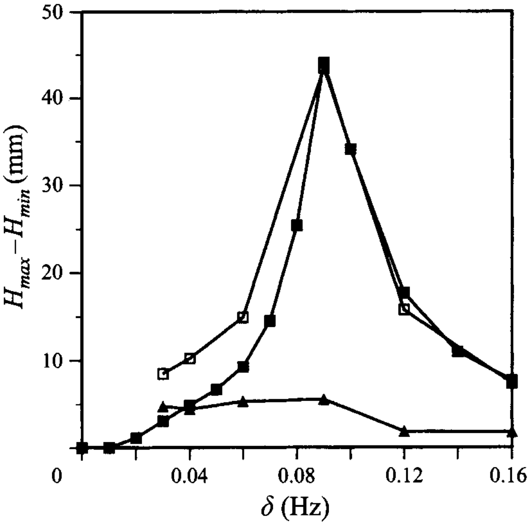

FIGURE 14. The effect of different sideband combinations on the modulated wave amplitude for 3.23 Hz oscillation with 5% intentional sideband (■, both sidebands added; □, lower sideband added; ▲, upper sideband added).

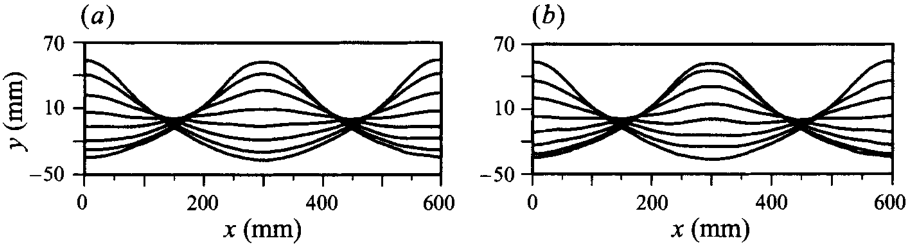

FIGURE 15. The detected wave profiles for a 3.23 Hz oscillation with a forcing amplitude of 2.65 mm. (a) During decreasing surface elevation at the centreline (from crest to trough at the centre). (b) During increasing surface elevation at the centreline (from trough to crest at the centre).

(crest) or minimum elevation (trough) and zero kinetic energy. With $\gamma = 0$ in equation (3.3), the existence of temporal symmetry is straightforward to show since equations (3.1) to (3.3) are invariant under the transformation $t \rightarrow -t$, $\phi \rightarrow -\phi$. However, non-zero dissipation modelled as $2\gamma\phi$ breaks the time-reversal symmetry in the forced standing waves studied here.

Wave profiles spanning one period are shown in figure 15 with decreasing and increasing elevation at the centreline. Even though the Faraday waves are temporally asymmetric, the moderate standing waves observed in the experiments have forms similar to the solution of Penney & Price (1952) – hardly discernible temporal asymmetry and nearly stationary profiles at the moment when either crest or trough is in the tank centre. These observations are also supported by our numerical results. However, forced and free standing waves become less similar when we increase the forcing amplitude. Symmetry breaking and nonlinear interaction lead to different wave forms of steep standing waves that have not been observed in previous experiments or analyses.

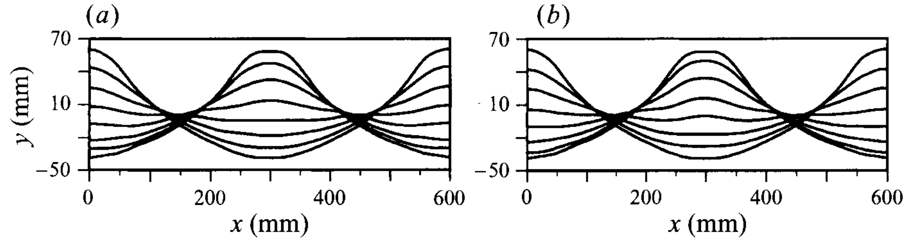

FIGURE 16. Same as figure 15 except that the forcing amplitude is 3.16 mm.

6. Steep standing waves: new wave forms

6.1. *Flat and dimpled crests*

Figure 16 displays a series of spatial wave profiles during a temporal period with forcing amplitude 3.16 mm. Compared to Faraday waves with the same frequency but less amplitude (figure 15), higher harmonics are more obvious in the wave profile and the crest of the maximum wave elevation is *flat*. Temporal symmetry is broken, but spatial symmetry is preserved – as in all of our experiments.

In figure 17, the maximum wave profile has evolved from a *flat* crest and features a *dimpled* crest for a larger forcing amplitude of 3.85 mm. The temporal asymmetry is more notable in the comparison between the increasing and decreasing crest phase at the tank centreline: the wave is more peaked where the surface elevation is increasing (part *b*). As soon as it achieves its maximum elevation and begins to decrease in height, the dimpled crest forms (part *a*). Previous computations of standing waves assumed that the maximum wave height occurs when the velocity is zero everywhere (zero kinetic energy). In these experiments, however, the maximum wave height with dimpled crest is never stationary, as the two protuberances of the wave crest are still rising when the velocity at the centreline is zero. Higher spatial harmonics of about four waves are also observed at time intervals 0.160 s, 0.468 s, and 0.524 s. Addition of Photo Flo does not alter the nature of these wave forms.

In figure 18, our experiments on standing-wave forms are recorded in p, q parametric space. Since these experiments are started from quiescent conditions, the displayed data are enclosed by the fitted/extrapolated neutral-stability curve. The parametric space is divided qualitatively into four regimes based on the respective wave forms: moderate waves, waves with flat crest, waves with dimpled crest, and breaking waves. Clearly, waves steepen when either the forcing amplitude is increased (q is increased), or the forcing frequency is decreased (p is increased within the unstable region). The same conclusion can be drawn for moderate waves from the response diagram, figure 7(*a*), albeit with more effort. Strong temporal asymmetry is present in the flat-crested, double-crested, and breaking regions.

6.2. *Numerical simulations of steep Faraday waves*

The computational method presented in §3.2 performed well for moderate waves. For larger forcing amplitude, however, it is difficult to obtain a stable wave amplitude because of numerical ('zigzag') instabilities. This higher-mode instability is due to time-marching and aliasing errors in our algorithm. Here, we include an additional dissipative/dispersive term $\gamma_H \phi_{sss}$ in the dynamic free-surface condition (3.12). This third-order derivative, estimated spectrally, is more effective in suppressing the higher-mode numerical instability than high-frequency filtering (Kransy 1986), five-point averaging (Longuet-Higgins & Cokelet 1976) and other damping terms with higher

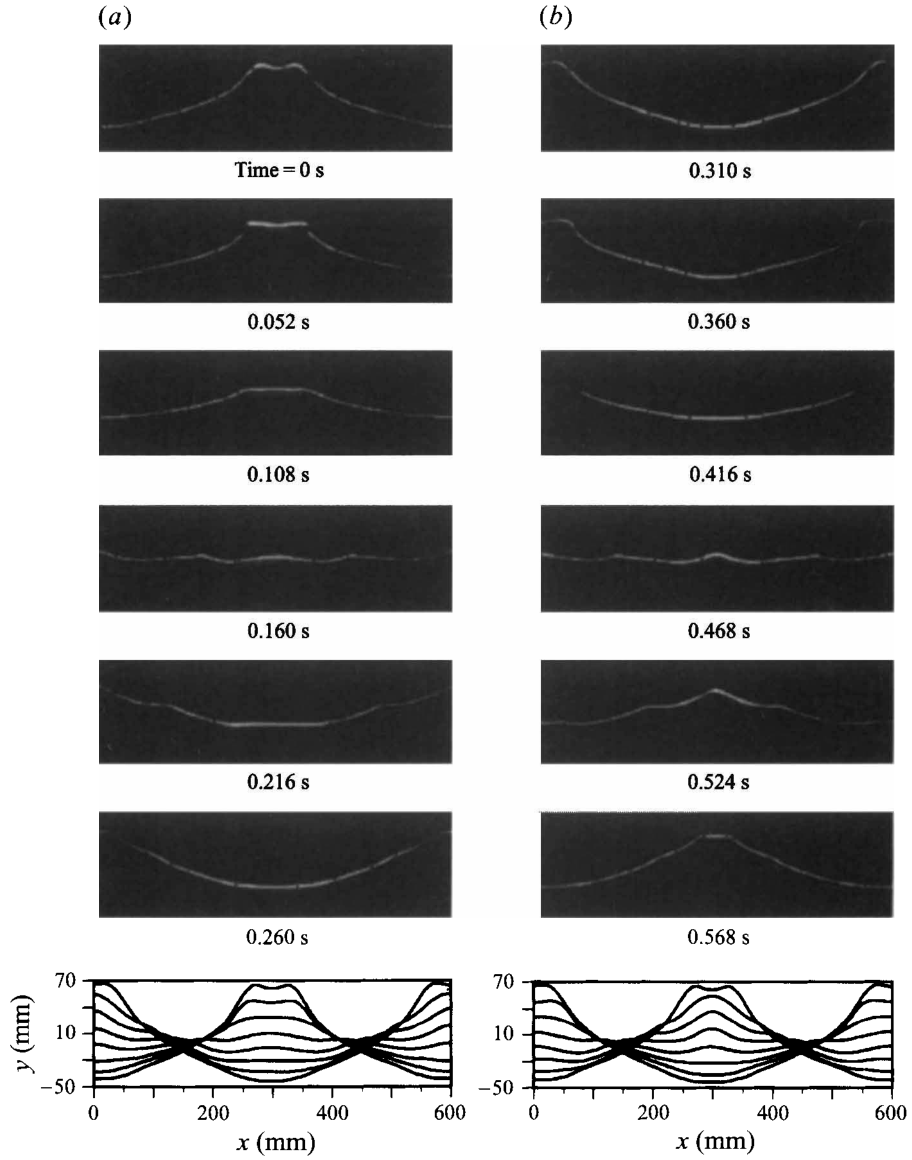

FIGURE 17. Standing wave profiles for a 3.23 Hz oscillation with a forcing amplitude of 3.85 mm. (*a*) The images and some detected profiles during decreasing surface elevation at the centreline (from crest to trough at the centre). (*b*) The images and some detected profiles during increasing surface elevation at the centreline (from trough to crest at the centre).

derivatives. In our computation, there is only minimal effect on the physical modes when this smoothing term is small: γ_H is chosen between 0.1% and 0.5% of the measured damping rate γ.

A simulated standing wave is shown in figure 19(*a*) for forcing amplitude 4.0 mm and forcing frequency 3.226 Hz ($\omega_f = 1.999\omega_N$). As the surface rises from the mean water level, the peak is more flat and even develops a dimple at a certain phase. However, it eventually has sharper curvature at its maximum elevation than does the experimental wave. The sharp crest remains as the elevation decreases towards

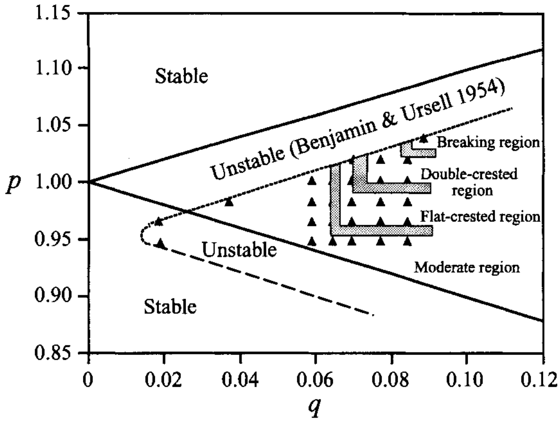

FIGURE 18. Location of the various wave forms in the p, q diagram: ——, inviscid subharmonic instability curves; -----, curve-fit to our experimental subharmonic–instability data; — —, curve extrapolated from our experimental data. Shaded areas are the approximate boundaries of four distinguished wave-form regions. (The exact boundaries cannot be determined from our limited data.) ▲, Experiments started from quiescent initial conditions.

the mean water level – the temporal symmetry is lost while the temporal periodicity is retained, as observed in the physical experiments of figure 17. Recall that in the physical experiments, a dimpled crest occurs at the maximum wave elevation and as the surface elevation decreases. In contrast, the numerical results exhibit a sharper crest at the maximum wave elevation and the dimpled crests are only obtained for increasing centreline elevation. This difference remains the same when the experimental forcing signal is used in our numerical study.

A surprising result from the calculations is the disappearance of the sharper crests at either higher or zero inverse Bond number. Figure 19(*c*, *d*) shows simulated wave profiles for $\kappa = 0$ (no surface tension) and figure 19(*e*, *f*) shows simulated wave profiles for $\kappa = 0.01$ (larger surface tension or shorter waves). In both cases, the wave form regains its similarity to Penney & Price (1952) even for very large forcing amplitude, without the dimples and sharp crests shown in figure 19(*a*, *b*) for $\kappa = 0.00081$.

6.3. *Temporal asymmetry and 2:1:2 internal resonance*

The standing-wave solutions derived by Penney & Price (1952) and Schwartz & Whitney (1981) are symmetric in time and the surface elevation can be represented by an even Fourier expansion $\cos t$, $\cos 2t, \cdots$. Although dissipation breaks temporal symmetry, damping itself does not explain the different wave forms in both experiments and numerical simulations. Instead, development of a second temporal harmonic, $\cos 4x \cos(2t + \varphi)$, leads to both asymmetry and a dimpled crest in the otherwise symmetric standing-wave solution: $A_1(x)\cos t + A_2(x)\cos 2t + \cdots$. In the present experiments, the new wave forms and the temporal asymmetry are indeed related to the magnitude and phase of the second harmonic (fourth harmonic in space).

As discussed by Miles & Henderson (1990), 2:1:2 internal resonance (the values represent forcing frequency : excited primary frequency : excited resonant frequency) occurs when two modes exist with a frequency ratio nearly 1:2, i.e. coexistence of subharmonic and synchronic modes with respect to the forcing frequency. Gu & Sethna (1987) shows that small frequency detuning and dissipation break the time-

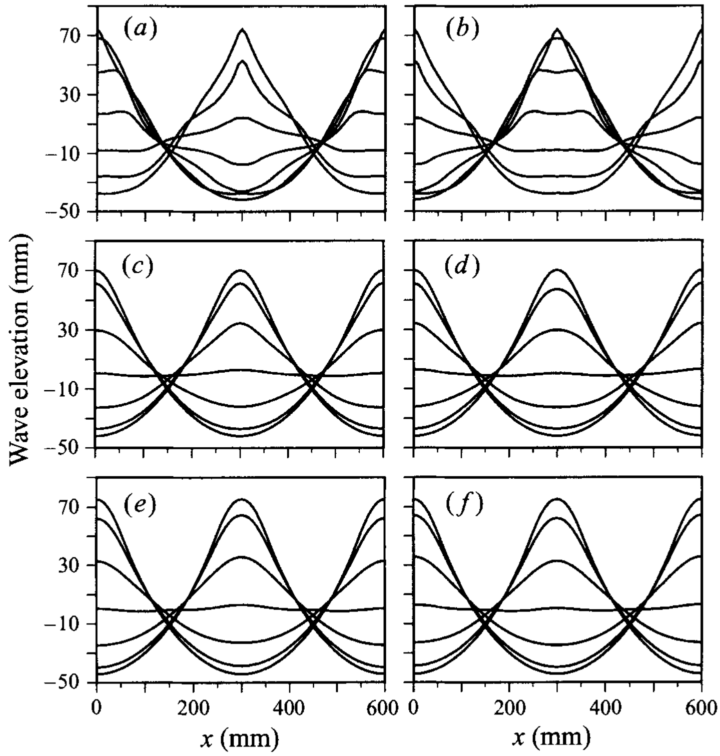

FIGURE 19. Simulated Faraday waves, forcing amplitude is 4.0 mm, forcing frequency is 3.226 Hz. (*a*) Decreasing crest elevation (from crest to trough at the centre), $\kappa = 0.00081$. (*b*) Increasing crest elevation, $\kappa = 0.00081$. (*c*) Decreasing crest elevation $\kappa = 0$. (*d*) Increasing crest elevation, $\kappa = 0$. (*e*) Decreasing crest elevation, $\kappa = 0.01$, (*f*) Increasing crest elevation, $\kappa = 0.01$.

reversal symmetry by shifting the phase of the resonant modes. However, it is assumed that the weakly nonlinear interaction of the two modes occurs at second order. The internal resonance for two-dimensional waves studied by Gu & Sethna requires capillary–gravity waves, similar to the Wilton ripple for progressive waves. Here, 2:1:2 internal resonance occurs for gravity waves: $\omega_8 : \omega_2 = 2$, where ω_8 is the frequency for the second temporal mode (four wavelengths in the tank) according to equation (3.8*b*) and ω_2 is ω_N. This resonance is analogous to the quartet interaction in progressive waves, and corresponds to the first violation of the uniqueness condition given by Tadjbakhsh & Keller (1960).

To estimate the 1:2 resonance and temporal asymmetry quantitatively, we first analyse our numerical results by applying DFT to the time series of wave elevation at the tank centre. The phases of the first and second harmonic are defined as θ_2 and θ_8. In Penney & Price (1952), the two harmonics are completely in phase ($\theta_8 - 2\theta_2 = 0$). Therefore $\theta_8 - 2\theta_2$ is used as an indication of the degree of asymmetry. Using different time windows for the same signal shows the standard deviation to be less than $\pm 0.03°$ in the phase estimates.

Shown in figure 20(*a*) is $\theta_8 - 2\theta_2$ for the calculated Faraday waves with and without surface tension. For moderate wave amplitudes, the asymmetry is negligible, evident from the small phase differences. Without surface tension, the frequency ratio between the forcing and the two natural modes is exactly 2:1:2. The phase difference ranges from 0° to −12.6° and there is no evident asymmetry nor strong second harmonics.

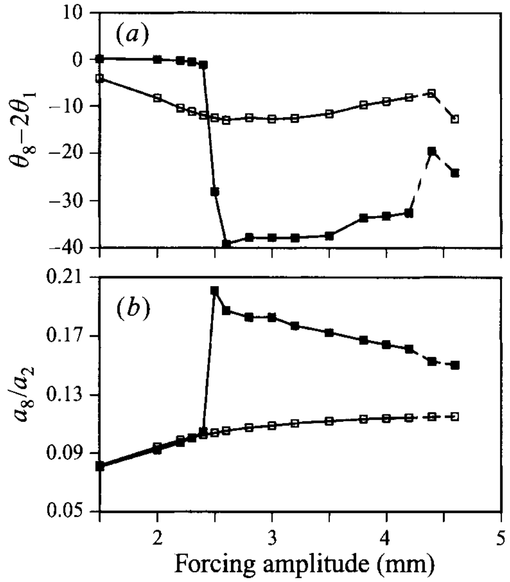

FIGURE 20. Phase difference $\theta_8 - 2\theta_2$ and dimensionless amplitude of the second harmonic a_8/a_2 for pure gravity wave ($\kappa = 0$) and capillary–gravity wave with small surface tension ($\kappa = 0.00081$). The forcing amplitude is shown along the horizontal axis and the forcing frequency is 3.22 Hz. The sharper crest appears at 2.5 mm forcing with $\kappa = 0.00081$. (□, $\kappa = 0$; ■, $\kappa = 0.00081$). The dashed portions of the curves represent simulations with questionable resolution.

No sharper, dimpled crest is observed even for a forcing amplitude of 4.6 mm. The dashed line shown for the two largest forcing amplitudes indicates computations of uncertain validity.

However, a small surface tension does cause large differences in the steep waves. Here, the effect of capillarity is critical because it causes a detuning among the forcing frequency and natural frequencies. With the same forcing frequency 3.226 Hz, the frequency ratio becomes 1.999:1:2.013 for a surface tension of 72 dynes cm^{-1} ($\kappa = 0.00081$). Computational results suggest a phase difference of about $-38°$ for forcing amplitudes larger than 2.5 mm and the large phase difference remains until the breaking-wave limit. Jumps at the same forcing amplitude also appear in figure 20(*b*) for the dimensionless amplitude of the second harmonic (a_8/a_2). These jumps occur with the appearance of sharper crests and asymmetric wave forms. With detuned forcing frequencies ($\omega_f < \omega_8$) and zero surface tension, we observe qualitatively similar waves; therefore the sharper crest observed in the computation only occurs for steep waves with small frequency detuning.

Even though the results of the physical experiments are not well reproduced in our simulations, analysis of the wave form with dimpled crest does show an increase in second-harmonic amplitude and a large, positive phase difference. Flat crests in the physical experiments correspond to $H\lambda^{-1} \approx 0.160$. For the numerical results in figure 20, the peaked wave form first appears at a wave steepness of 0.1536 (forcing amplitude is 2.5 mm). Both are far less than the extreme steepness 0.208 for standing waves (Schwartz & Whitney 1981).

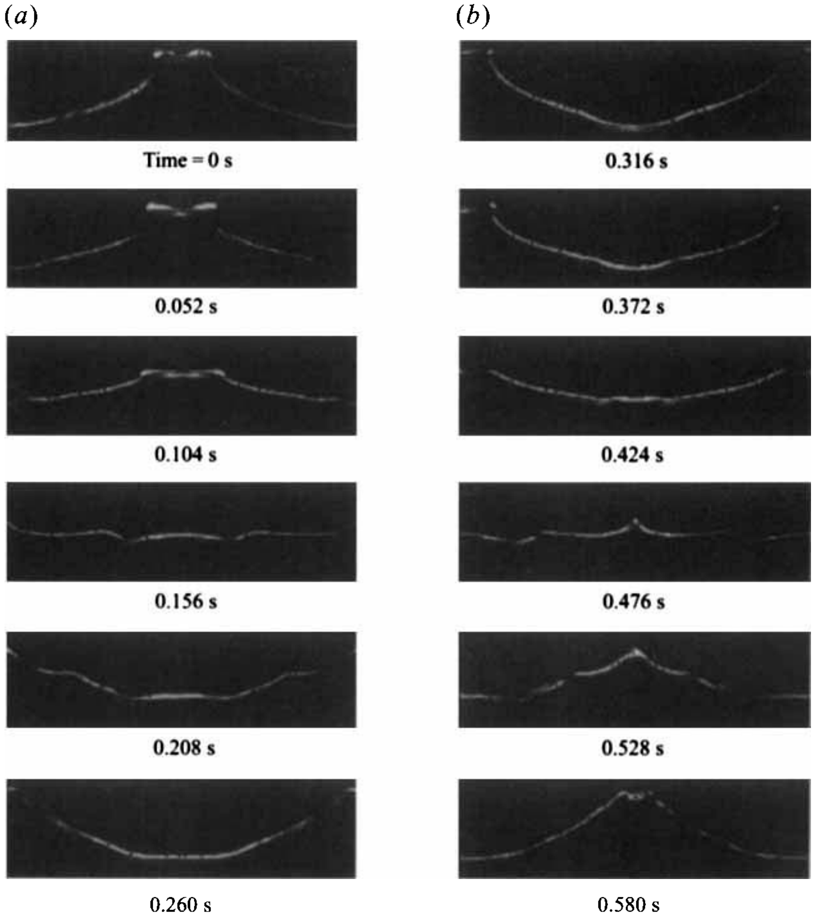

FIGURE 21. Same as figure 17 except that the forcing amplitude is 4.04 mm, the forcing frequency is 3.17 Hz, and the edge-detected profiles are not shown.

7. Breaking standing waves

In Taylor (1953), the extreme standing waves are three-dimensional. In our experiments with a tank aspect ratio of 10:1, the new wave form remains two-dimensional up to incipient breaking, corresponding to a steepness $H\lambda^{-1}$ of 0.216. The extreme wave steepness is larger than the numerical estimate of $H\lambda^{-1} \approx 0.2$ by Mercer & Roberts (1992). This agrees with previous conclusions that capillarity can increase the extreme steepness for free standing waves (Schultz & Vanden-Broeck 1990).

Experimental wave profiles over a temporal period are shown in figure 21 for waves with incipient breaking. The forcing amplitude is 4.04 mm and the forcing frequency is 3.17 Hz. The wave height here is about 130 mm. Aside from the small breaking that occurs at the sharper crest at $t = 0.580$ s, the wave profile is similar to the non-breaking standing wave presented in figure 17. Overturning waves with small plunging breakers to each side of the centreline are also present with the dimpled crest at the beginning of the series. The waveform is still spatially symmetric about the centreline and the same breaking events occur at the two ends of the container with a half-period lag (see time = 0.372 s).

The numerical experiments using the third-derivative smoothing function can be extended to steepness larger than 0.20. However, higher harmonics are not suppressed indefinitely and the computation is only extended to approximately 20 wave periods depending on the initial conditions. This is consistent with the superharmonic instability that occurs at the extreme steepness for free standing waves (Mercer & Roberts 1992) and the observed incipient breaking with $H\lambda^{-1} > 0.216$.

8. Concluding remarks

Here, we have investigated analytically, numerically, and experimentally several aspects of standing waves. As recognized in the literature (H&M for example), damping-rate models are inadequate, so measured values are discussed and used in the weakly nonlinear theory and the numerical predictions. An examination of the p, q diagram reveals that the contact line significantly increases the viscous natural frequency, shifting the neutral-stability curve downward. Effects of the contact line are shown two ways: by conducting experiments in wider rectangular containers and by the addition of Photo Flo; both reduce the contact-line effects dramatically. With Photo Flo as a contact-line lubricating agent, the viscous effect dominates the threshold forcing amplitude and frequency, and the neutral-stability curve agrees more closely with the theory of H&M.

The response diagram exhibits strong 'soft spring' nonlinearity through hysteresis, revealed by varying the forcing frequency in discrete steps with a fixed forcing amplitude. Experiments with and without Photo Flo show that this hysteresis depends strongly on the forcing amplitude and the contact-line effect. The wave amplitudes of the Faraday waves are in agreement with our numerical simulation and reasonable agreement with H&M's theory.

Large wave modulations are observed in the experiments in the high-frequency forcing regime. The modulations in the physical experiments are explained by the influence of ambient noise due to the contact line and noise in the forcing signal. The asymptotic estimate of the 'sideband resonance' through forcing noise compares favourably with controlled experiments and very favourably with numerical simulations. The addition of Photo Flo reduces the ambient noise level caused by the contact line; however, intentional sideband forcing precipitates a return of the modulations even with Photo Flo.

We have observed previously unpredicted steep standing waves, although moderate Faraday wave forms are similar to the solution of Penney & Price (1952). Flat and dimpled crests appear in the forced standing waves for larger wave amplitudes and the kinetic energy of the standing wave is never zero. The sequential wave profiles show strong temporal asymmetry. Moreover, the numerical analysis demonstrates that a small detuning between forcing and natural frequencies, either introduced directly or induced by a small surface tension, leads to a wave with much sharper crest. Even though its profile does not resemble the wave with a dimpled crest in the physical experiments, both are strongly asymmetric in time and only emerge at finite wave amplitude. The growing second harmonic and strong asymmetry in these different wave forms indicate 2:1:2 internal resonance among the first and second harmonics, analogous to 'quartet' interaction. In the physical experiments, we have shown one manner in which two-dimensional Faraday waves break – overturning plungers to each side of the crest. The maximum steepness for the new wave forms exceeds the theoretical predictions for gravity standing waves, in agreement with the conclusion of Schultz & Vanden-Broeck (1990) for free standing waves with surface tension.

Further studies will focus on two issues. First, a more quantitative study is necessary on the exact contact-line mechanism responsible for the viscous-frequency shift, modulations, and the role of Photo Flo, in a manner similar to Ting & Perlin (1995). Second, to understand more about the steep standing waves and breaking, the Faraday wave with 2:1:2 internal resonance requires more detailed study that includes the 'quartet' interaction. We plan to extend the experiments to three dimensions (using smaller aspect-ratio basins) and pursue the applicability of observed wave forms to SAR signatures.

This research was supported by the Office of Naval Research partially under contract number N00014-93-1-0867 and partially under the University Research Initiative Ocean Surface Processes and Remote Sensing at the University of Michigan, contract number N00014-92-J-1650.

Appendix. Sideband resonance

It is evident from our experiments that modulation occurs for $\Omega > 0$. Therefore only the solution with the + sign is available in equation (3.16). Assuming $A_1 = b_1 e^{iT\Delta} + b_2 e^{-iT\Delta}$, we obtain the following algebraic equations from equation (3.20)

$$(-\Delta + i\Gamma - \Omega - 2G|A_0|^2)\, b_1 - (F_0 + GA_0^2)\, b_2^* = F_0 A_0^*, \tag{A 1}$$

$$-(F_0 + GA_0^{*2})\, b_1 + (\Delta - i\Gamma - \Omega - 2G|A_0|^2)\, b_2^* = F_0 A_0, \tag{A 2}$$

where b_2^* is the complex conjugate of b_2 and J is the determinant of the coefficient matrix

$$\begin{aligned} J &= \left[(\Omega + 2G|A_0|^2)^2 - (\Delta - i\Gamma)^2 - |F_0 + GA_0^2|^2\right] \\ &= 4\left(F_0^2 - \Gamma^2\right)^{1/2}\left[\left(F_0^2 - \Gamma^2\right)^{1/2} - \Omega\right] - \Delta^2 + 2i\Delta\Gamma. \end{aligned} \tag{A 3}$$

Using the steady solution for A_0, we get solutions for b_1 and b_2:

$$b_{1,2} = \frac{[\pm\Delta - \Omega - 2G|A_0|^2 - i\Gamma]A_0^* + (F_0 + GA_0^2)A_0}{4\left(F_0^2 - \Gamma^2\right)^{1/2}\left[\left(F_0^2 - \Gamma^2\right)^{1/2} - \Omega\right] - \Delta^2 \pm 2i\Delta\Gamma} F_0 = P_{1,2}\cos\theta + iQ_{1,2}\sin\theta. \tag{A 4}$$

The coefficients P_1, P_2 and Q_1, Q_2 are

$$P_1 = \frac{(\Delta + R_1) - iR_2}{J} F_0 a_0; \quad Q_1 = \frac{(-\Delta + R_3) - iR_4}{J} F_0 a_0;$$

$$P_2 = \frac{(-\Delta + R_1) - iR_2}{J^*} F_0 a_0; \quad Q_2 = \frac{(\Delta + R_3) - iR_4}{J^*} F_0 a_0,$$

where

$$R_1 = \Omega + \frac{(\Omega - 2F_0)\left(F_0^2 - \Gamma^2\right)^{1/2} + \Gamma^2}{F_0}; \quad R_3 = R_1 - 2\Omega;$$

$$R_2 = \Gamma \frac{F_0 - \Omega + \left(F_0^2 - \Gamma^2\right)^{1/2}}{F_0}; \quad R_4 = R_2 - 2\Gamma.$$

Here J^* is the complex conjugate of J. The resonant modulation frequency as defined in equation (3.24) can be estimated accurately by seeking the maximum of $b_{1,2}$ in (A 4). It turns out that neglecting damping is a good approximation and the frequency estimate (3.24) is sufficiently accurate.

REFERENCES

AHLERS, G., HOHENBERG, P. C. & LUCKE, M. 1985 Thermal convection under external modulation of the driving force. I. The Lorenz model. *Phys. Rev.* A **32**, 3493–3518.

AMICK, C. J. & TOLAND, J. F. 1987 The semi-analytic theory of standing waves. *Proc. R. Soc. Lond.* A **411**, 123–137.

BENJAMIN, T. B. & SCOTT, J. C. 1979 Gravity-capillary waves with edge constraints. *J. Fluid Mech.* **92**, 241–267.

BENJAMIN, T. B. & URSELL, F. 1954 The stability of the plane free surface of a liquid in vertical periodic motion. *Proc. R. Soc. Lond.* A **225**, 505–515.

BRYANT, P. J. & STIASSNIE, M. 1994 Different forms for nonlinear standing waves in deep water. *J. Fluid Mech.* **272**, 135–156.

CHEN, B. & SAFFMAN, P. G. 1979 Steady gravity-capillary waves on deep water I. Weakly nonlinear waves. *Stud. Appl. Maths* **60**, 183–210.

CHEN, X.-N. & WEI, R.-J. 1994 Dynamic behaviour of a non-propagating soliton under a periodically modulated oscillation. *J. Fluid Mech.* **259**, 291–303.

CRAIK, A. D. D. & ARMITAGE, J. 1995 Faraday excitation, hysteresis and wave instability in a narrow rectangular wave tank. *Fluid Dyn. Res.* **15**, 129–143.

DECENT, S. P. & CRAIK, A. D. D. 1995 Hysteresis in Faraday resonance *J. Fluid Mech.* **293**, 237–268.

DODGE, F. T., KANA, D. D. & ABRAMSON, H. N. 1965 Liquid surface oscillations in longitudinally excited rigid cylindrical containers. *AIAA J.* **3**, 685–695.

FULTZ, D. 1962 An experimental note on finite amplitude standing gravity waves. *J. Fluid Mech.* **13**, 195–212.

GRAHAM-EAGLE, J. 1983 A new method for calculating eigenvalues with applications to gravity-capillary waves with edge constraints. *Proc. Camb. Phil. Soc.* **94**, 553–564.

GU, X. M. & SETHNA, P. R. 1987 Resonant surface waves and chaotic phenomena. *J. Fluid Mech.* **183**, 543–565.

HART, J. E. 1991 Experiments on planetary scale instabilities. In *Nonlinear Topics of Ocean Physics, Proc. Fermi Summer School* (ed. A. R. Osborne and L. Bergamasco), pp. 271–312. North-Holland.

HENDERSON, D. M. & MILES, J. W. 1990 Single-mode Faraday waves in small cylinders. *J. Fluid Mech.* **213**, 95–109 (referred to as H&M herein).

HENDERSON, D. M. & MILES, J. W. 1994 Surface-wave damping in a circular cylinder with a fixed contact line. *J. Fluid Mech.* **275**, 285–299.

HOCKING, L. M. 1987 The damping of capillary-gravity waves at a rigid boundary. *J. Fluid Mech.* **179**, 253–266.

KRASNY, R. 1986 A study of singularity formation in a vortex sheet by the point-vortex approximation. *J. Fluid Mech.* **167**, 65–93.

LONGUET-HIGGINS, M. S. & COKELET, E. D. 1976 The deformation of steep surface waves on water: I. A numerical method of computation. *Proc. R. Soc. Lond.* A **350**, 1–26.

MERCER, G. N. & ROBERTS, A. J. 1992 Standing waves in deep water: their stability and extreme form. *Phys. Fluids A* **4**, 259–269.

MERCER, G. N. & ROBERTS, A. J. 1994 The form of standing waves on finite depth water. *Wave Motion* **19**, 233–244.

MILES, J. W. 1967 Surface-wave damping in closed basins. *Proc. R. Soc. Lond.* A **297**, 459–475.

MILES, J. W. 1976 Nonlinear surface waves in closed basins. *J. Fluid Mech.* **75**, 419–448.

MILES, J. W. 1984 Nonlinear Faraday resonance. *J. Fluid Mech.* **146**, 285–302.

MILES, J. W. 1990 Capillary-viscous forcing of surface waves. *J. Fluid Mech.* **219**, 635–46.

MILES, J. W. 1993 On Faraday waves. *J. Fluid Mech.* **248**, 671–683.

MILES, J. W. 1994 Faraday waves: rolls versus squares. *J. Fluid Mech.* **269**, 353–371.

MILES, J. W. & HENDERSON, D. M. 1990 Parametrically forced surface waves. *Ann. Rev. Fluid Mech.* **22**, 143–165.

MILNER, S. T. 1991 Square patterns and secondary instabilities in driven capillary waves. *J. Fluid Mech.* **225**, 81–100.

NAGATA, M. 1989 Nonlinear Faraday resonance in a box with a square base. *J. Fluid Mech.* **209**, 265–284.

PENNEY, W. G. & PRICE, A. T. 1952 Finite periodic stationary gravity waves in a perfect liquid. *Phil. Trans. R. Soc. Lond.* A **244**, 254–284.

PERLIN, M. & HAMMACK, J. 1991 Experiments on ripple instabilities. Part 3. Resonant quartet of the Benjamin-Feir type *J. Fluid Mech.* **229**, 229–268.

PERLIN, M., LIN, H. & TING, C. 1993 On parasitic capillary waves generated by steep gravity waves: an experimental investigation with spatial and temporal measurements. *J. Fluid Mech.* **255**, 597–620.

PHILLIPS, O. M. 1977 *The Dynamics of the Upper Ocean.* Cambridge University Press, 2nd edn.

SAAD, Y. & SCHULTZ, M. H. 1986 GMRES: a generalized minimal residual algorithm for solving nonsymmetric linear systems. *SIAM J. Sci. Statist. Comput.* **7**, 856–869.

SCHULTZ, W. W., HUH, J. & GRIFFIN, O. M. 1994 Potential energy in steep and breaking waves. *J. Fluid Mech.* **278**, 201–228.

SCHULTZ, W. W. & VANDEN-BROECK J. M. 1990 Computations of nonlinear standing waves. *Bull. Am. Phys. Soc.* **35**, 2290.

SCHWARTZ, L. W. & WHITNEY, A. K. 1981 A semi-analytic solution for nonlinear standing waves in deep water. *J. Fluid Mech.* **107**, 147–171.

TADJBAKHSH, I. & KELLER, J. B. 1960 Standing surface waves of finite amplitude. *J. Fluid Mech.* **8**, 442–451.

TAYLOR, G. I. 1953 An experimental study of standing waves. *Proc. R. Soc. Lond.* A **218**, 44–59.

TING, C. L. & PERLIN, M. 1995 Boundary conditions in the vicinity of the contact line at a vertically oscillating upright plate: an experimental investigation. *J. Fluid Mech.* **295**, 263–300.

VANDEN-BROECK, J. M. & SCHWARTZ, L. W. 1981 Numerical calculation of standing waves in water of arbitrary uniform depth. *Phys. Fluids* **24**, 812–815.

VINJE, T. & BREVIG, P. 1981 Numerical simulation of breaking waves. *Adv. Water Resources* **4**, 77–82.

VIRNIG, J.C., BERMAN, A.S. & SETHNA, P.R. 1988 On three-dimensional nonlinear subharmonic resonant surface waves in a fluid: part II. experiments. *Trans. ASME* E: *J. Appl. Mech.* **55**, 220–224.